Journal of Geophysical Research: Oceans

RESEARCH ARTICLE
10.1029/2018JC014345

Oceanic Heat Delivery to the Antarctic Continental Shelf: Large-Scale, Low-Frequency Variability

André Palóczy[1], Sarah T. Gille[1], and Julie L. McClean[1]

[1]Scripps Institution of Oceanography, University of California, San Diego, La Jolla, CA, USA

Key Points:
- The contributions from eddy advection, eddy stirring, and mean flow advection to the total onshore heat transport vary regionally
- The time-mean component governs the seasonal variability of the total heat transport and largely cancels the eddy component
- Circumpolar heat transports and total heat content of the Antarctic continental margin follow SAM, but ENSO prevails in West Antarctica

Supporting Information:
- Supporting Information S1

Correspondence to:
A. Palóczy,
apaloczy@ucsd.edu

Citation:
Palóczy, A., Gille, S. T., & McClean, J. L. (2018). Oceanic heat delivery to the Antarctic continental shelf: Large-scale, low-frequency variability. *Journal of Geophysical Research: Oceans*, *123*. https://doi.org/10.1029/2018JC014345

Received 6 JUL 2018
Accepted 24 SEP 2018
Accepted article online 1 OCT 2018

Abstract Onshore penetration of oceanic water across the Antarctic continental slope (ACS) plays a major role in global sea level rise by delivering heat to the Antarctic marginal seas, thus contributing to the basal melting of ice shelves. Here the time-mean (Φ^{mean}) and eddy (Φ^{eddy}) components of the heat transport (Φ) across the 1,000-m isobath along the entire ACS are investigated using a 0.1° global coupled ocean/sea ice simulation based on the Los Alamos Parallel Ocean Program (POP) and sea ice (Community Ice CodE) models. Comparison with in situ hydrography shows that the model successfully represents the basic water mass structure, with a warm bias in the Circumpolar Deep Water layer. Segments of on-shelf Φ, with lengths of O(100–1,000 km), are found along the ACS. The circumpolar integral of the annually averaged Φ is O(20 TW), with Φ^{eddy} always on-shelf, while Φ^{mean} fluctuates between on-shelf and off-shelf. Stirring along isoneutral surfaces is often the dominant process by which eddies transport heat across the ACS, but advection of heat by both mean flow-topography interactions and eddies can also be significant depending on the along- and across-slope location. The seasonal and interannual variability of the circumpolarly integrated Φ^{mean} is controlled by convergence of Ekman transport within the ACS. Prominent warming features at the bottom of the continental shelf (consistent with observed temperature trends) are found both during high-Southern Annular Mode and high-Niño 3.4 periods, suggesting that climate modes can modulate the heat transfer from the Southern Ocean to the ACS across the entire Antarctic margin.

Plain Language Summary The Antarctic Circumpolar Current (ACC), carrying warm Circumpolar Deep Water (CDW), flows eastward in the deep Southern Ocean basin usually far from cooler Antarctic coastal waters. However, when the ACC does approach the Antarctic coast, CDW can supply heat to the floating edges of the Antarctic ice cap. We use a realistic computer model of the global ocean and sea ice to study these processes. The model indicates that winds, ocean eddies, and current interactions with the seafloor all contribute to moving heat toward Antarctica. Seasonal wind changes around Antarctica affect the heat transport (HT) near the surface and the HT due to current-seafloor interactions but not so much the HT due to eddies. Over multi-year periods, some of the changes in the HT are related to climate variability taking place in the tropics and around Antarctica. Both the processes responsible for bringing heat to the Antarctic coast and the variability of this heat delivery represent knowledge needed to improve computer model simulations of the Antarctic ice cap's melting. In turn, improving these simulations is likely to reduce uncertainties in projections of sea level rise, allowing for the development of adaptation and mitigation policies that better address global societal impacts.

1. Introduction

Basal melting of ice shelves has emerged as the primary driver of continental ice mass loss in Antarctica (e.g., Liu et al., 2015; Rignot et al., 2013). This process has major societal ramifications, as it modulates global sea level rise and its possible acceleration (Nerem et al., 2018; Shepherd et al., 2018). All of the water masses occupying the continental shelf may provide heat to drive melting, including fresh and cold (but seasonally warming) Antarctic Surface Water (AASW) and cold Antarctic Shelf Bottom Water (e.g., Dinniman et al., 2016). However, the warmest shelf water mass is modified Circumpolar Deep Water (mCDW; 2–4 °C above the in situ freezing point), which is formed when offshore water with higher CDW content enters the continental shelf and is stirred and mixed by the coastal circulation. mCDW is thought to dominate basal melt at seasonal through decadal (Cook et al., 2016; Jenkins et al., 2016; Thoma et al., 2008) time scales. Melting induced by mCDW occurs in regions where it has access to the subglacial cavities of ice shelves, such as in the Amundsen and Bellingshausen Seas (e.g., Jenkins et al., 2016). This view is further supported by the similarities between the

Table 1
Recent Modelling Estimates of Time-Averaged, Circumpolarly Integrated Heat Transport Across the 1,000-m Isobath (Φ^{circ}, Positive On-Shelf)

Study	Φ^{circ}	Resolution	Atmospheric forcing	Ice shelves	Tides	Freshwater
Dinniman et al. (2015)	~50 TW	10 km	2010 reanalysis (cyclic)	Yes	No	Yes
Goddard et al. (2017)	~25–33 TW	4–6 km	Coupled atmosphere	No	No	Yes
Stewart et al. (2018)	~27 TW	<1 km	2011–2012 reanalysis	No	Yes	Yes
This study	22.2 TW	3.8–4.7 km	Time-varying CORE-II	No	No	No

Note. All ocean models were coupled to associated sea ice models. The two values on the Goddard et al. (2017) study refer to their control and doubled atmospheric CO_2 experiments. The value for Dinniman et al. (2015) is an average of the last five years of their simulation, where the atmospheric forcing was based on 2010 fields, applied cyclically every model year. The value for the present study is also a 5-year average but is over 2005–2009, as our simulation was forced with the interannually varying CORE-II atmospheric product. CORE = Coordinated Ocean-ice Reference Experiment.

spatial structure of the observed trends in ice-shelf thickness (Paolo et al., 2015) and water mass properties in the Weddell and Ross Seas and in West Antarctica: where ice shelves are thinning, both CDW and Antarctic Shelf Bottom Water are warming, and the CDW core on the adjacent continental slope is shoaling (Schmidtko et al., 2014). Further, recent observations in East Antarctica reveal that mCDW also reaches the Totten (Greenbaum et al., 2015; Rintoul et al., 2016; Silvano et al., 2016) and Moscow University (Silvano et al., 2017) ice shelves through deep cross-shelf troughs, with sufficient heat content to induce melt rates comparable to those found in West Antarctica (Greenbaum et al., 2015; Rignot et al., 2013).

At mesoscales and submesoscales, evidence has shown that eddies of O(1–5 km) are prime contributors to the onshore mass and heat transports across the continental slope (e.g., Graham et al., 2016; Nøst et al., 2011; Stewart & Thompson, 2013, 2015b, 2016; Stewart et al., 2018, hereafter SKM18), likely via eddy stirring of temperature along isopycnals (Stewart & Thompson, 2016; SKM18). The background Antarctic Slope Current/Undercurrent (ASC/ASUC) flow also plays an important role (Chavanne et al., 2010; Peña-Molino et al., 2016; Walker et al., 2013). In particular, the ASUC vertical structure has been observed to lift the pycnocline above the sill depth of some cross-slope troughs in the southeastern Weddell Sea through thermal wind shear (Chavanne et al., 2010), suggesting that it could play a similar role in other marginal seas. Bottom Ekman transport (Peña-Molino et al., 2016; Wåhlin et al., 2012) and inertial penetration of the Antarctic Circumpolar Current (ACC) onto the shelf (Dinniman & Klinck, 2004; Dinniman et al., 2011) may also be important on the continental slope and shelf break.

Part of the heat delivered to the shelf break by eddies and the background mean flow is channeled farther onshore by cross-shelf troughs, pathways that have been most extensively observed in West Antarctica (e.g., Couto et al., 2017; Gunn et al., 2018; Moffat et al., 2009; Nakayama et al., 2013; Walker et al., 2007, 2013; Wåhlin et al., 2013, 2016; Zhang et al., 2016). Onshore heat transports within these troughs are estimated to be of O(1–10 TW) based on in situ observations (Assmann et al., 2013; Ha et al., 2014; Kalén et al., 2015; Martinson & McKee, 2012; Walker et al., 2007; Wåhlin et al., 2013) and idealized or regional numerical simulations (e.g., Graham et al., 2016; St-Laurent et al., 2013). At the circumpolar scale, numerical models have simulated on-shelf transports in the 20–50-TW range across the 1,000-m isobath (Dinniman et al., 2015; Goddard et al., 2017; SKM18; Table 1).

Although progress regarding the importance of heat transport pathways at mesoscales and submesoscales has been encouraging, observed long-term trends in shelf temperature (Cook et al., 2016; Jenkins et al., 2016; Schmidtko et al., 2014) suggest that cross-shelf edge heat transport may occur over a range of spatiotemporal scales. Enhanced warming on the Antarctic continental shelf has recently been simulated in global high-resolution climate models (Goddard et al., 2017; Spence et al., 2014, 2017), and results suggest that large-scale atmospheric modes such as the Southern Annular Mode (SAM) may be important drivers of interannual coastal variability at the circumpolar scale. Indeed, Armitage et al. (2018) show that the joint effects of the SAM and the El Niño/Southern Oscillation (ENSO) modulate coastal sea level and the strength of the ASC at seasonal and interannual time scales, which likely influences cross-isobath heat transport. Some of the fastest melting ice shelves in West Antarctica (those located between the East Ross and West Amundsen Seas) appear to be particularly sensitive to strong El Niños (Paolo et al., 2018). In contrast, farther north in the West Antarctic Peninsula, Martinson et al. (2008) observed a much higher volume of mCDW on the shelf in 1999 (strong La Niña and strong SAM+) relative to 1998 (strong El Niño and moderate SAM+). While a strong La Niña combined with SAM+ events maximizes the response of the Amundsen Sea Low's strength (Fogt et al.,

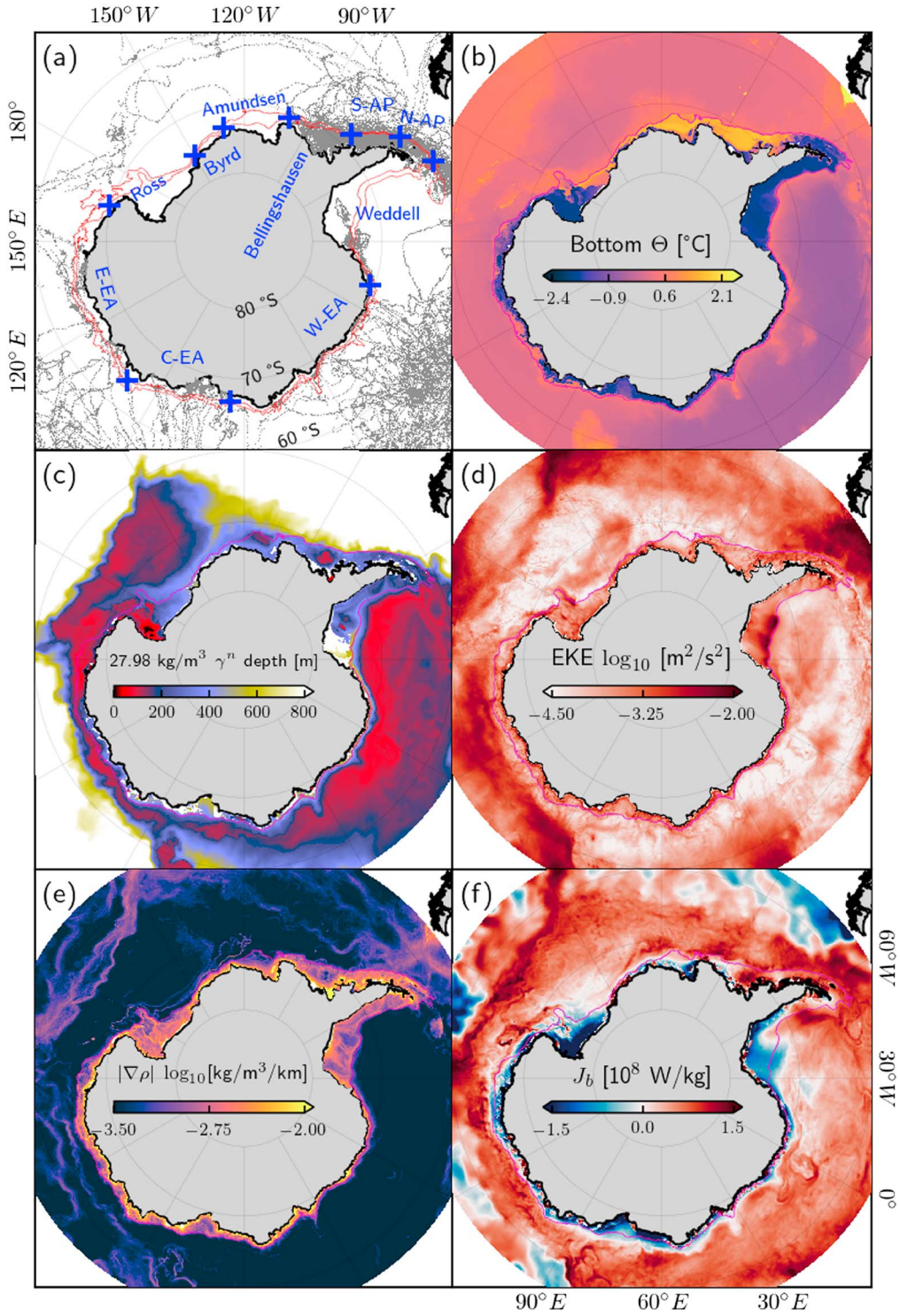

Figure 1. Definition of the subregions analyzed, distribution of in situ data and simulated variables over the Antarctic continental slope. (a) Segments chosen to partition the Antarctic continental slope. The red contours are the 800- and 2,500-m isobaths, and blue crosses demarcate boundaries between segments. Gray dots indicate the locations of the in situ hydrographic profiles (Marine Mammals Exploring the Oceans Pole to Pole data set). S-AP and N-AP = South and North Antarctic Peninsula. E-EA, C-EA, and W-EA = East, Central, and West portions of East Antarctica. (b-f) Time-averaged (2005–2009) horizontal simulated fields. (b) Bottom Conservative Temperature (Θ). (c) Depth of the 1,027.98 kg/m^3 neutral density surface. (d) Logarithm of depth-averaged Eddy Kinetic Energy (EKE). (e) Logarithm of depth-averaged lateral density gradient magnitude ($|\nabla\rho|$). (f) Surface buoyancy flux (J_b), positive where the ocean becomes more buoyant. The magenta contour in (b–f) is the 1,000-m isobath.

2011, their Figure 5e), the effects of each El Niño/La Niña on the Amundsen Sea Low's strength are different, and this has been suggested to modulate the basal melt of ice shelves (Paolo et al., 2018). This fragmented picture indicates gaps in our understanding of the possible links between climate modes and the oceanic heat transports around the Antarctic margin.

To our knowledge, previous work on this problem using eddy-permitting ocean models has only examined short-duration simulations (SKM18), decadal averages (Spence et al., 2014), or the statistically steady state of the system under semi-idealized atmospheric forcing (Dinniman et al., 2015; Goddard et al., 2017; Spence et al., 2014). SKM18 found that over most of the Antarctic margin, the tidal and mean onshore heat transports roughly cancel at the shelf break, and the net onshore heat transfer is accomplished by the eddy component in an eddy-resolving model. However, the short duration of their simulation (13 months) precluded an analysis of interannual variability. Investigating the response of the time-varying, large-scale flow to realistic forcing has the potential to improve our understanding and projections of sea level rise and the global overturning circulation (Ruan et al., 2017; Stewart & Thompson, 2013; Thompson et al., 2014).

The central aim of this paper is to quantify the contribution of large-scale pathways to the heat budget of the Antarctic continental margin and the mechanisms associated with its low-frequency variability (seasonal through multidecadal). To achieve this, we perform a circumpolar heat budget analysis along the Antarctic continental margin in a global simulation with realistic atmospheric forcing and coupled ocean and sea ice models. We first describe the model (section 2) and observational tools (section 3). Next, we evaluate model biases by comparing the simulated fields to in situ observations in section 4. We then examine the time-averaged along-isobath (section 5.1.1) and cross-isobath (section 5.1.2) structures of the cross-isobath heat transport, followed by its seasonal (section 5.2) and interannual (section 5.3) variabilities and its potential drivers. Finally, in section 6, we summarize our results, discuss some of their implications, and present our main conclusions.

2. The Global 0.1° POP Simulation

We analyze modeled fields derived from a global coupled ocean/sea ice simulation (McClean et al., 2018) based on the Los Alamos Parallel Ocean Program 2 (POP2; e.g., Smith et al., 2010) and Community Ice CodE 4 (CICE4; e.g., Hunke et al., 2010) in the Community Earth System Model framework. The simulation is configured on a global nominal 0.1° tripole grid with 3.8–4.7 km horizontal resolution on the Antarctic shelf and 42 vertical levels, with vertical spacing varying from 10 m near the surface to 500 m near the bottom. Partial bottom cells (Pacanowski & Gnanadesikan, 1998) are used to improve the discretization of the bottom topography. The simulation spanned the period 1948–2009 and was forced with the corrected interannually varying air-sea fluxes from the Coordinated Ocean-ice Reference Experiment version 2 (CORE-II; Large & Yeager, 2009). We analyze the model output only after 1958, allowing for an 11-year spin-up period. Vertical mixing of temperature and salinity by nonlocal convection (when the mixed layer is gravitationally unstable) and local diabatic processes was implemented with the K-Profile Parameterization (Large et al., 1994). Subgrid scale horizontal mixing is parameterized using biharmonic operators, whose associated coefficients for momentum and tracers vary spatially with the cube of the grid cell size. At the equator, the horizontal mixing coefficients for momentum and tracers have values of -2.7×10^{10} and -3.0×10^{9} m^4/s, respectively.

In order to perform regional analyses of the water mass structure and heat transports, we divide the circumpolar Antarctic continental slope (ACS) into 10 segments: Ross Sea, Byrd Coast, Amundsen and Bellingshausen Seas, south and north portions of the Western Antarctic Peninsula, Weddell Sea, and West, Central, and East portions of East Antarctica (Figure 1a). Following Goddard et al. (2017), we choose the 1,000-m isobath as a proxy for the Antarctic Slope Front (ASF; Figures 1b–1f). We define the ACS as the closed control volume bounded by the 800- and 2,500-m isobaths (Figure 1a). The ACS volume was used to calculate spatial averages of the in situ observations and to ensure that the discrete cross-ASF heat transport calculations are consistent with a numerically closed heat budget (see supporting information Figure S1).

Realistic representation of mesoscale and submesoscale eddies is made difficult by the small internal deformation radius, which typically decreases from 10 to 4 km across the ACS (e.g., Moffat et al., 2009; Stewart & Thompson, 2013). A horizontal resolution of ~1 km is needed to fully resolve eddies on the continental slope and shelf (Graham et al., 2016; St-Laurent et al., 2013; Stewart & Thompson, 2015b; SKM18). Our simulation's resolution is therefore eddy-permitting, and we limit ourselves to analyzing the low-frequency (multiannual to multidecadal, spanning 1959–2009) variability of the large-scale, O(100–1,000 km) cross-isobath transports.

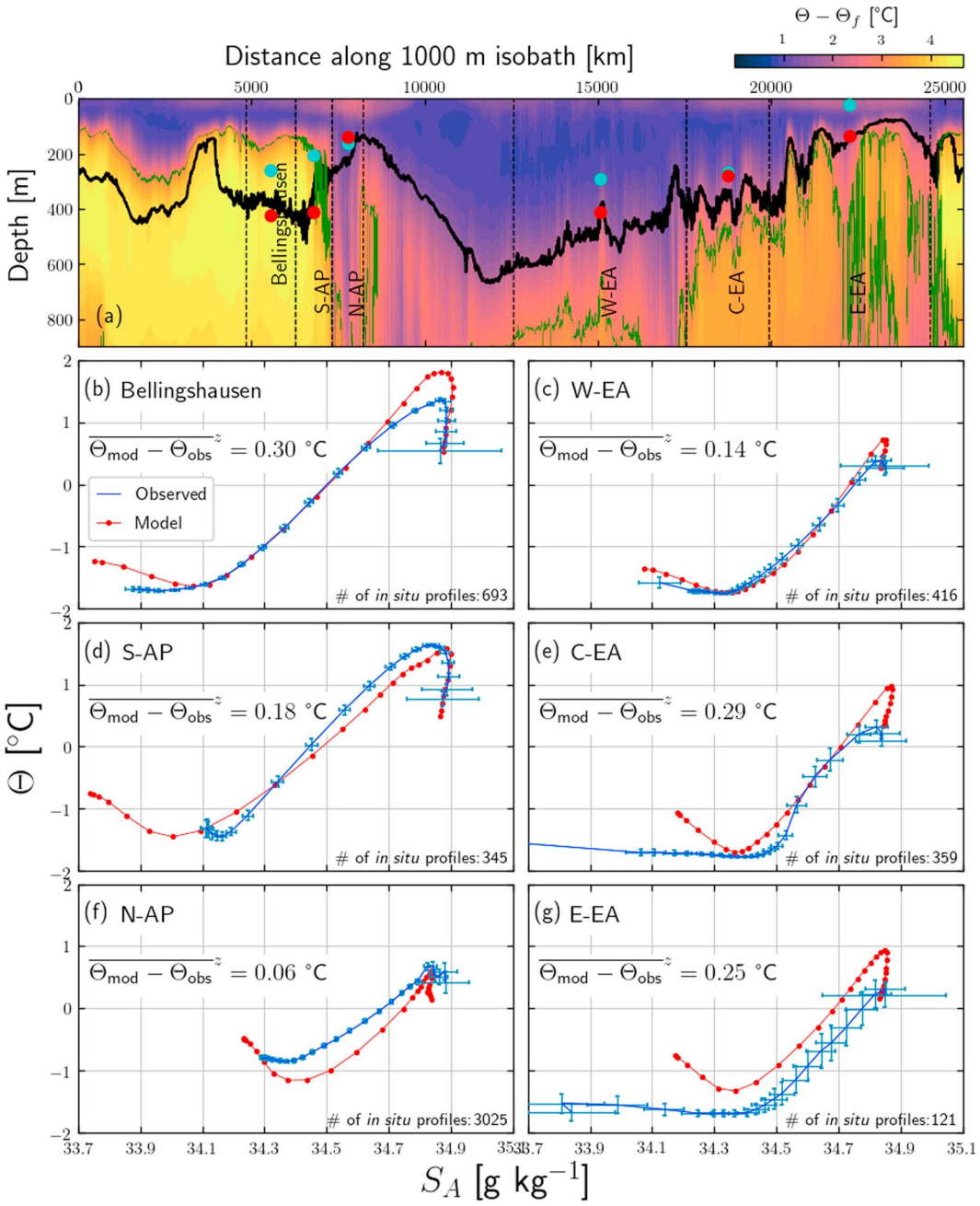

Figure 2. Model-data comparison of the time-averaged (2005–2009) water mass structure along the Antarctic continental slope. (a) Section of simulated Conservative Temperature above the freezing point ($\Theta - \Theta_f$) along the 1,000-m isobath. The green contour is the $\Theta - \Theta_f = 3$ °C isoline. The black contour is the 1,027.98 kg/m^3 simulated isoneutral, whose spatially averaged depth within each segment is indicated by the red (model) and blue (observed) dots. The only segment where the simulated and observed isoneutral depths are statistically indistinguishable is C-EA. (b–g) Conservative Temperature-Absolute Salinity (Θ-S_A) diagrams. The blue error bars indicate the 95% confidence intervals about the observed Θ and S_A mean profiles. The number of observed profiles on each segment and the depth-averaged difference between simulated and observed temperatures ($\overline{\Theta_{mod} - \Theta_{obs}}^z$) are also shown on each panel. Spatial averages are calculated only for six of the segments of the Antarctic continental slope defined in Figure 1a. S-AP = South Antarctic Peninsula; N-AP = North Antarctic Peninsula; E-EA = East portion of East Antarctica, C-EA = Central portion of East Antarctica; W-EA = West portion of East Antarctica.

Evidently, the circumpolar integral of the total cross-isobath heat transport is constrained by the area integral of the surface heat flux within the closed isobath, which will necessarily account for the similarities and differences of the circumpolar heat transport among independent simulations (Table 1). The segment-averaged eddy component of the heat transport is O(1 MW/m) in our simulation (Figure S6), as is SKM18's (their Figure 2), even though our eddy kinetic energy levels are typically a factor of 10 smaller along the 1,000-m isobath (Figures 1d and 7e) and our model has no tidal circulation.

Two other important limitations to point out are the absence of tides and ice shelves. Regarding tides, SKM18 find that although the eddy heat transport is more important along the continental slope, tides contribute a larger onshore heat transport than eddies at the shelf break in their eddy-resolving simulation. Ice shelves play a role in the heat budget of the system both directly as a boundary sink and indirectly as a source of potential energy for the coastal circulation, which may in turn modify the advective heat transports across the shelf break and their convergences/divergences within the continental shelf. We find that a heat transport of 14 TW into the circumpolar system is required to account for Rignot et al.'s (2013) estimate of 1,325 Gt/year of ice-shelf meltwater production, using a latent heat of melt of $L_f = 334$ kJ/kg (e.g., Jourdain et al., 2017). This amounts to 71% of the 19.7 TW we find for the time-averaged (1959–2009) circumpolar onshore heat transport, and this heat must be released to the atmosphere in the absence of thermodynamically active ice shelves (the heat tendency term averages to a small number in the long-term mean). Also, the missing density gradients due to the absence of ice shelves and freshwater imply that some of the heat that is available on the continental slope but is not brought onto the shelf in this simulation might be if ice shelves were introduced, since their effect on the circulation can be substantial (e.g., Dinniman et al., 2015; Jourdain et al., 2017; St-Laurent et al., 2013). In a future contribution, we will compare our present results with a global eddy-resolving POP/CICE simulation (1–2-km resolution on the Antarctic continental margin) with climatological freshwater fluxes of ice-shelf melting and iceberg calving derived from observations (Hammond & Jones, 2016).

3. The MEoP CTD Observations

We evaluate the realism of the simulated fields using Conservative Temperature (Θ) and Absolute Salinity (S_A) profiles derived from the Marine Mammals Exploring the Oceans Pole to Pole (MEoP) data set (e.g., Roquet et al., 2014; Figure 1a). Each tagged animal carries a Conductivity, Temperature, and Depth Satellite Relay Data Logger and records data during the ascent of each dive. Only the deepest dive in a 6-hr interval is transmitted, with 10 to 25 data points per profile (Roquet et al., 2014). The accuracy of the ARGOS geo-positioning system is ~5 km. Different calibration procedures are applied to the postprocessed data depending on the availability of nearby shipboard observations and the water masses sampled in the profile (Roquet et al., 2011); therefore, error estimates for individual deployments have not been attempted (Roquet et al., 2014). As a result, the postprocessed in situ profiles have variable instrumental errors and calibration uncertainties. Profiles measured in 2007 or more recently are estimated to be accurate to ±0.03 °C for in situ temperature (T) and ±0.05 psu for practical salinity (S_p), while pre-2007 profiles have accuracies of 0.1 °C and 0.1 psu (Roquet et al., 2014). Although only 10% of the profiles used in our analyses were measured before 2007, we estimate uncertainties in results derived from the observed profiles by making the most conservative assumptions, namely, ±0.1 °C for T and ±0.1 for S_p (Roquet et al., 2014).

4. The Circumpolar Water Mass Structure

Intrusions of mCDW are ultimately regulated by the availability of CDW on the continental slope. Therefore, prior to calculating the circumpolar heat budget, it is desirable to evaluate the realism of the simulated water mass structure along the ACS, especially the depth and temperature of the CDW. To achieve this, we compare simulated and observed Θ and S_A profiles along the ACS to evaluate the representation of the water mass structure across individual segments of the ACS. The observed profiles are interpolated onto the model vertical grid, and then simulated and observed profiles are both time-averaged for the 2005–2009 period and spatially-averaged within the segments that have a higher density of MEoP profiles (Bellingshausen, S-AP, N-AP, W-EA, C-EA, and E-EA; see Figure 1a). This approach enables the spatial averaging of the in situ profiles necessary to obtain statistically meaningful comparisons with the simulated fields.

The section of simulated Conservative Temperature above the freezing point ($\Theta - \Theta_f$; Figure 2a) reveals warm CDW (up to 4 °C above the freezing point) and overlying cold AASW. The simulated 1,027.98-kg/m^3 isoneutral surface (a surface of same neutral density γ^n), which is a proxy for the simulated CDW layer, is 0–200 m deeper

than observed (red and blue dots in Figure 2a). In the CDW layer, the model overestimates Θ by ∼0.5 °C in the Bellingshausen Sea and in East Antarctica (Figures 2b, 2c, 2e, and 2g).

This near-ubiquitous warm bias in simulated CDW is comparable to that found in the Amundsen Sea shelf by Jourdain et al. (2017) in their regional implementation of the Nucleus for European Modeling of the Ocean (NEMO) model, which is an ocean/sea ice model with static ice shelves. They attributed the warm bias of ∼0.5-1.1 °C to a more stratified thermocline caused by an overestimated amplitude of the sea ice formation/melting seasonal cycle. This intensified sea ice seasonal cycle is also found in the present simulation (Figure S2) and is a known bias of global simulations under CORE-II Inter-Annual Forcing (IAF) forcing (Downes et al., 2015). The biases in the cold and fresh end of the $\Theta - S_A$ curve (the AASW layer) are less consistent. The thermocline stratification is well represented in most segments, with simulated and observed Θ-S_A curves often being statistically indistinguishable away from the CDW and AASW layers (Figures 2b–2g).

Although this model-observation comparison is encouraging, the AASW and CDW layers are the dominant sources of oceanic heat. We thus expect the model biases in the vertical water mass structure to impact our estimates of cross-isobath heat transport. The depth-averaged difference between the simulated and observed temperatures ($\overline{\Theta_{\mathrm{mod}} - \Theta_{\mathrm{obs}}}^{z}$) is up to 0.3 °C or 11% of $\overline{\Theta_{\mathrm{obs}} - \Theta_f}^{z}$, where $\bar{\bullet}^z$ indicates a depth average. With the circulation unchanged, a 10% warm bias translates into a 10% heat transport bias (equation (1)), for example, a ∼2-TW error for a 20-TW simulated circumpolar heat transport. However, the cross-slope velocity bias is unknown, and it is therefore unclear whether the real on-shelf heat transport is being overestimated or underestimated.

5. The Cross-Shelf Break Heat Transport Along the Antarctic Continental Margin

We define the total heat transport relative to the freezing point as

$$\Phi(y) \overset{\mathrm{def}}{=} \rho C_p \int_{-h}^{0} u(y,z')[\theta(y,z') - \theta_f]\,\mathrm{d}z', \tag{1}$$

where y and z are the along-isobath and vertical coordinates, respectively, and z' is a dummy integration variable parallel to z; $u(y,z)$ is the cross-isobath velocity (positive onshore); C_p is the heat capacity of seawater; ρ is the potential density referenced to 0 dbar; $\theta(y,z)$ is the potential temperature referenced to 0 dbar; and θ_f is the θ at which seawater freezes. In the presentation of the simulated results, we replace Θ with θ, because θ is the model temperature variable. The density ρ is set to 1,026 kg/m^3, and C_p is set to 3,996 J kg^{-1} °C^{-1} to be consistent with the simulation. The product $u(y,z,t)\theta(y,z,t)$ is accumulated at each model time step. However, since neither the quantity $\theta(y,z,t)-\theta_f(y,z,t)$ nor the product $u(y,z,t)\theta_f(y,z,t)$ were saved, we follow Goddard et al. (2017) and set θ_f to the minimum freezing temperature found along the 1,000-m isobath in the simulation ($\theta_f = -2.64$ °C). This means that the quantity $\rho C_p[\theta(y,z) - \theta_f]$ must be interpreted as an upper bound (i.e., warmest value) for the melting potential of the intruding water masses. Setting θ_f to its minimum value also ensures that the volume and heat transports are in the same direction, facilitating the interpretation of our results.

We break Φ into eddy (Φ^{eddy}) and time-mean (Φ^{mean}) components, that is, $\Phi^{\mathrm{eddy}} \overset{\mathrm{def}}{=} \Phi - \Phi^{\mathrm{mean}}$, where Φ^{mean} is calculated offline using the monthly averaged velocity and temperature fields. This decomposition separates the eddying variability (any motion with period shorter than 30 days) from the lower-frequency variability. Motions such as barotropic Kelvin waves (Kusahara & Ohshima, 2014; Spence et al., 2017) and partially resolved mesoscale eddies project onto Φ^{eddy}, while Φ^{mean} captures very low-frequency continental shelf wave modes (Kusahara & Ohshima, 2009), Ekman transports, and seasonal variability, including its interannual changes over the analyzed period (1959–2009). We point out that since the outputs for the full time span of the simulation are available in monthly averaged fields, any averaging period that is a multiple of a month is possible. The choice of 1 month (as opposed to, e.g., 1 year or 1959–2009) is made in order to avoid including the seasonal variability in Φ^{eddy}. Seasonality is instead projected on Φ^{mean}.

In order to examine possible physical mechanisms associated with Φ^{eddy}, we follow Stewart and Thompson (2016; hereafter ST16) and further split Φ^{eddy} into contributions from eddy advection ($\Phi^{\mathrm{eddy}}_{\mathrm{adv}}$) and eddy stirring ($\Phi^{\mathrm{eddy}}_{\mathrm{stir}}$), with

$$\Phi^{\mathrm{eddy}}_{\mathrm{adv}} \overset{\mathrm{def}}{=} \rho C_p \int_{-h}^{0} \overline{u^{\mathrm{eddy}}}(z') \left[\bar{\theta}(z') - \theta_f\right] \mathrm{d}z', \tag{2}$$

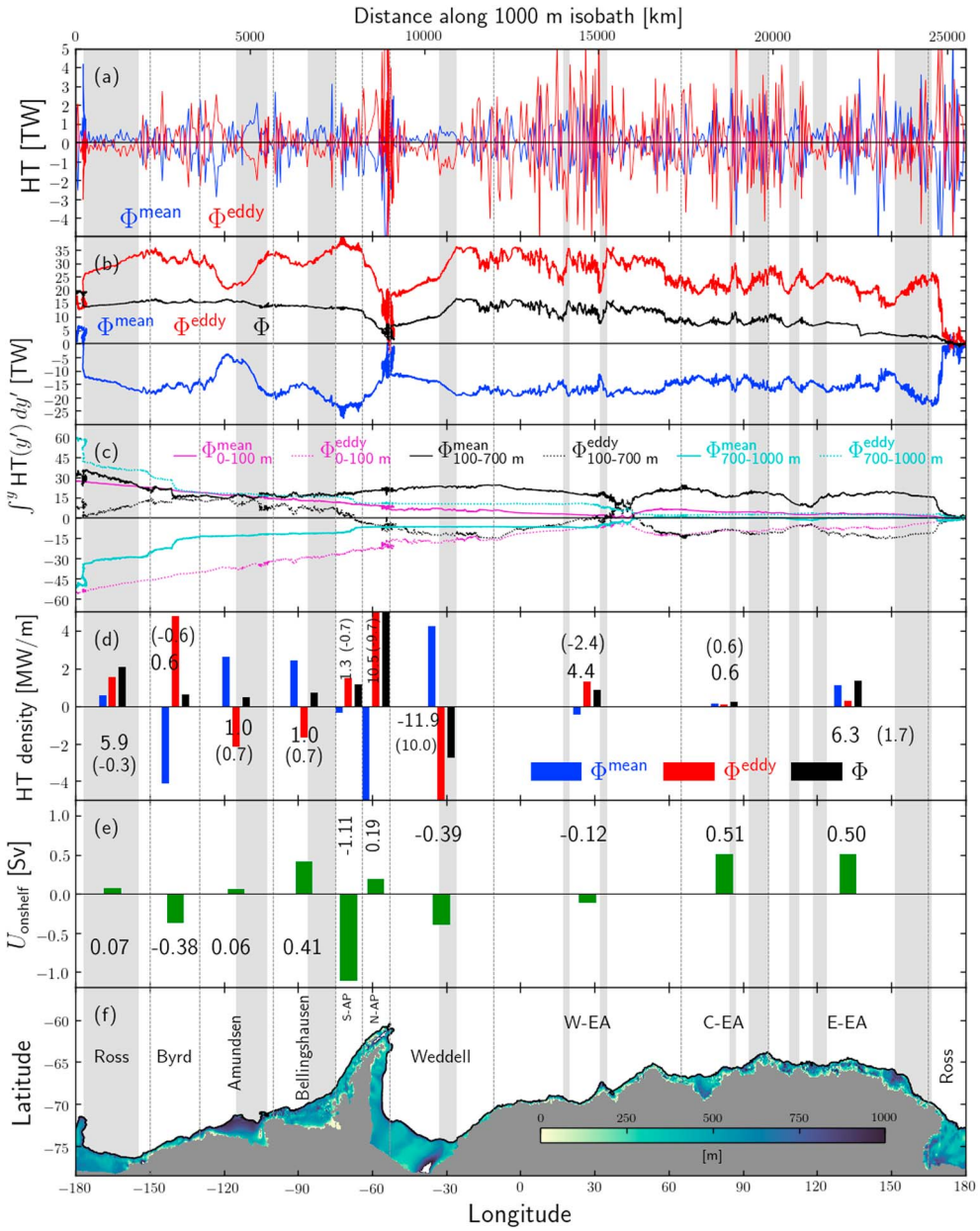

Figure 3. Time-averaged (1959–2009) cross-isobath heat transport (HT; positive on-shelf) along the Antarctic continental slope (1,000-m isobath). (a) Vertically integrated (0–1,000 m) mean (Φ^{mean}) and eddy (Φ^{eddy}) components of the total cross-1,000-m HT, Φ. (b) Along-isobath cumulative sums (from east to west) of Φ^{mean}, Φ^{eddy}, and Φ. (c) Mean and eddy contributions to the heat transport integrated within the top (0–100 m), middle (100–700 m), and bottom (700–1,000 m) layers, also cumulatively summed from east to west. (d) Along-isobath averages of Φ, Φ^{mean}, and Φ^{eddy} for each segment (vertical bars); Φ integrated over the segment (nonbracketed numbers); and along-shelf convergence of the along-shelf HT within the segment (bracketed numbers). (e) Total cross-isobath volume transport within each segment ($U_{onshelf}$, positive on-shelf). (f) Bottom topography inshore of the 1,000-m isobath (black line). The vertical-dashed lines demarcate the segments defined in Figure 1a. The gray-shaded areas mark some of the heat intrusion pathways that are O(100 km) or larger. The cumulative sums in (b) and (c) are calculated westward starting from 180° E in order to follow the prevailing direction of the shelf and slope currents. EA = East portion of East Antarctica, C-EA = Central portion of East Antarctica; W-EA = West portion of East Antarctica.

where $u^{\text{eddy}} = -\partial_z \psi^{\text{eddy}}$, and ψ^{eddy} is the Neutral Density Transformed Eulerian Mean overturning streamfunction (Stewart & Thompson, 2015a), defined as

$$\psi^{\text{eddy}} \overset{\text{def}}{=} \frac{\bar{\beta}\,\overline{u' S_p'} - \bar{\alpha}\,\overline{u'\theta'}}{\bar{\beta}\,\partial_z \overline{S_p} - \bar{\alpha}\,\partial_z \bar{\theta}}, \tag{3}$$

where $\bar{\alpha} = \alpha(\overline{S_p}, \bar{\theta}, p)$ is the thermal expansion coefficient, $\bar{\beta} = \beta(\overline{S_p}, \bar{\theta}, p)$ is the haline contraction coefficient, u is the cross-isobath transport, S_p is practical salinity, and θ is potential temperature. Overbars ($\bar{\bullet}$) indicate averaging in the along-isobath direction (along the length of the segment considered) and in time (over each month). Primes ($\bullet'$) indicate departures from this average.

Equation (3) is analogous to the eddy thickness fluxes of the Gent-McWilliams parameterization (Gent & McWilliams, 1990) in models that do not resolve eddies. Motivated by this analogy, we follow ST16 and define $\Phi^{\text{eddy}}_{\text{stir}}$ as the difference $\Phi^{\text{eddy}} - \Phi^{\text{eddy}}_{\text{adv}}$. In this decomposition, the quantity $\Phi^{\text{eddy}}_{\text{adv}}$ is the heat carried by eddy motions via advection of warmer or colder water masses across the isobath (i.e., the eddy overturning circulation) and is associated with a nonzero thickness (hence volume) flux. In contrast, $\Phi^{\text{eddy}}_{\text{stir}}$ is not linked to any net volume transport and therefore measures the heat transport due to stirring of potential temperature along isoneutral surfaces (ST16).

5.1. The Time-Mean (1959–2009) Circumpolar Structure

5.1.1. Along-Isobath Distribution of On-Shelf Heat Transports

We now search for persistent on-shelf heat penetration pathways on the Antarctic continental margin by examining the time-averaged (1959–2009) spatial structure of the mean (Φ^{mean}) and eddy (Φ^{eddy}) components of the total (Φ) heat transport across the 1,000-m isobath. Both Φ^{mean} and Φ^{eddy} have rich spatial structures that generally mirror one another (Figures 3a and 3b). The net circumpolar transports Φ^{mean} and Φ^{eddy} (averaged over 1959–2009) are 4.6 and 15.1 TW, respectively, for a total of 19.7 TW. The total heat transport averaged over the 2005–2009 period is 22.2 TW, comparable to other recent modeling estimates (Table 1).

Figures 3a–3c show the time-averaged Φ^{mean}, Φ^{eddy}, and Φ as functions of distance along the 1,000-m isobath. The widespread cancellation between onshore and offshore heat transport in along-isobath bands is evident, especially in East Antarctica. There is also consistent cancellation between Φ^{mean} and Φ^{eddy}, which leaves small onshore or offshore Φ residuals, sometimes along O(100–1,000 km) segments (Figure 3b). For example, in the Bellingshausen, East Amundsen, and east end of E-EA (later called the Oates subsegment), Φ is onshore (gray stripes and black line in Figure 3b). These hot spots of enhanced heat transport are often collocated with abrupt topographic features (Figure 3f), as previously found in modeling studies (Graham et al., 2016; Goddard et al., 2017; SKM18) and observations (e.g., Ha et al., 2014; Kalén et al., 2015).

In addition to these sites of preferred cross-isobath heat transport, the along-shelf divergence of the heat transport across adjacent segments of the Antarctic continental shelf (Figure 3d) appears to be an important pathway for heat delivery (where there is convergence) or sequestration (where there is divergence). The along-shelf divergence of the heat transport partly or almost completely compensates for the incoming offshore heat in some segments (Ross, Byrd, S-AP, N-AP, and W-EA), while in other segments, along-shelf convergence adds to the oceanic on-shelf heat input (Amundsen, Bellingshausen, C-EA, and E-EA; Figure 3d). For instance, an average of 2.76 TW enters the Amundsen segment from the Byrd segment, but only 2.08 TW exits the Amundsen segment across its boundary with the Bellingshausen segment. Combined with the incoming 0.96 TW crossing the 1,000-m isobath, there is a total 1.64 TW of advective heat convergence within the Amundsen Sea segment (in the 1959–2009 mean). Rodriguez et al. (2016) find a 2005–2009 average total heat transport convergence of 1.15 TW in the Amundsen segment (their Table 2) in the coarser (1/6°) Southern Ocean State Estimate. This is comparable to the 1.78 TW in the 2005–2009 POP average (not shown).

The time-averaged on-shelf volume transport U_{onshelf} within each segment is typically less than 1 Sv and does not appear to follow the time averages of Φ^{mean}, Φ^{eddy}, or Φ in a regular fashion across segments (Figures 3d and 3e). In time, however, U_{onshelf} turns out to be very strongly anticorrelated with Φ^{eddy} in all segments at a 10-month lag and moderately correlated with Φ^{mean} in most segments at a 10-month lag (Table S1). While the mechanism involved in the strong control of Φ^{eddy} by U_{onshelf} is unclear, the small net U_{onshelf} is consistent with an isobath-following mean geostrophic flow and suggests that eddy momentum flux convergence is playing

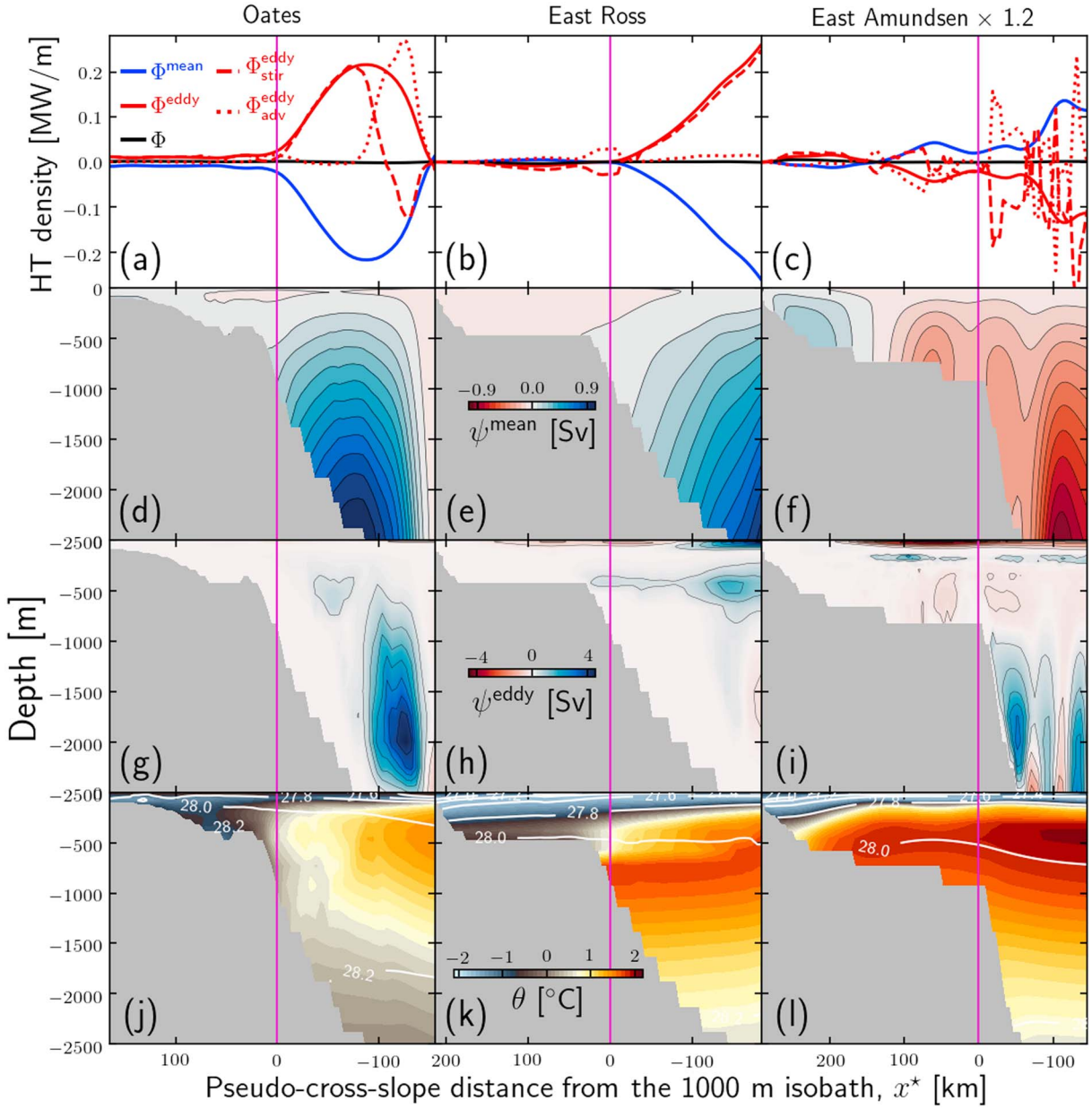

Figure 4. Time-averaged (1959–2009) and along-shelf-averaged sections of the components of the heat transport (HT; positive onshore), mean, and eddy overturning stream functions and potential temperature (θ) at subsegments Oates (135° to 150° E), East Ross (180° to 155° W), and East Amundsen (115° to 110.5° W), see Figure 1a. (a–c) Time-mean (Φ^{mean}), eddy advection Φ^{eddy}_{adv}, eddy stirring Φ^{eddy}_{stir}, and total eddy ($\Phi^{eddy} = \Phi^{eddy}_{adv} + \Phi^{eddy}_{stir}$) contributions to the total pseudo-onshore heat transport per unit along-shelf length, Φ. To facilitate comparison, the HT components for the East Amundsen (c) subsegment are multiplied by 1.2. (d–f) Mean overturning stream function, $\psi^{mean}(x^\star, z)$. (g–i) Eddy overturning stream function, $\psi^{eddy}(x^\star, z)$. The abscissa on all panels is a pseudo-cross-isobath coordinate, $x^\star$ (see section 5.1.2). Red indicates clockwise circulation, which tends to be linked to positive (onshore) HT. Note that the existence of open streamfunction contours is a result of the along-shelf averaging. (j–l) Cross-slope potential temperature, θ with the $\gamma^n - 1,000$ isoneutrals overlaid (white contours). The vertical magenta lines across the panels indicates the along-shelf mean position of the 1,000-m isobath.

an important part in the cross-isobath overturning circulation, as noted by SKM18 in the East Antarctic sector of their simulation.

Except for the Ross, C-EA, and E-EA segments, the segment-averaged Φ^{mean} and Φ^{eddy} are in opposite directions. Breaking down the vertically integrated transport in surface (0–100 m), bottom (700–1,000 m), and interior (100–700 m) layers reveals that Φ^{mean} and Φ^{eddy} partially cancel each other throughout most of the system, especially in the top and bottom layers (Figure 3c). SKM18 find a similar cancellation between the net onshore tidal and offshore mean heat fluxes in their eddy- and tide-resolving simulation. The contribution of

the surface Ekman transport to the onshore circumpolar heat transport can be estimated as

$$\Phi_{\mathrm{Ek}}^{\mathrm{mean}} = -L_{\mathrm{circ}} C_p (\Theta - \Theta_f) \frac{\tau^y_{\mathrm{circ}}}{f}, \tag{4}$$

where $\Theta - \Theta_f = 1.43$ °C is the Conservative Temperature above the freezing point averaged in the top 25 m (Figure 2a), $f = -1.36 \times 10^{-4} s^{-1}$ is the inertial frequency, and $\tau^y_{\mathrm{circ}} = -0.036$ Pa is the along-isobath wind stress. These values are along-isobath circumpolar averages, $C_p = 3996$ J kg^{-1} °C^{-1} is the specific heat capacity of seawater, and $L_{\mathrm{circ}} = 25,520$ km is the total length of the 1,000-m isobath. This yields an estimate of $\Phi_{\mathrm{Ek}}^{\mathrm{mean}} = 33.7$ TW. This suggests that the time-mean heat transport in the upper 100 m (Figure 3c) is mostly due to Ekman transport, as SKM18 find in their simulation.

5.1.2. Cross-Slope Overturning Circulation and Heat Transport Structure

In contrast with an idealized, along-shelf-uniform continental shelf/slope model (e.g., ST16), flow properties in POP around the Antarctic continental margin are very noisy and sensitive to the along-shelf location being examined. We therefore present cross-shelf profiles and sections of along-shelf averaged quantities (within subregions of the segments in Figure 1a), rather than at specific along-shelf locations. In this section we discuss three representative subsegments as case studies (Figure 4), occasionally referring to the other subsegments (Figures S9 and S10). The cross-slope heat transport components and the mean (ψ^{mean}) and eddy (ψ^{eddy}) streamfunctions are plotted as functions of the pseudo-cross-isobath coordinate $x^\star$, defined by SKM18 as

$$x^\star(h_0) \overset{\mathrm{def}}{=} \frac{1}{L_y} \iint_{h<h_0} 1 \, dA, \tag{5}$$

where $h(x, y)$ is the bottom depth, $z = -h_0$ is a specific isobath, and dx, dy, and $dA = dx\, dy$ are cross-isobath, along-isobath, and horizontal area elements, respectively. Ultimately, $x^\star$ is the distance along the profile of $h(x)$ averaged within each subsegment's length L_y. As such, it captures the mean cross-slope topography for each segment. We examine the along-shelf averages of the mean streamfunction

$$\psi^{\mathrm{mean}}(x^\star, z) \overset{\mathrm{def}}{=} \int_z^0 \bar{u}(x^\star, z')\, \mathrm{d}z', \tag{6}$$

where, again, $\bar{\bullet}$ indicates an along-isobath and time average, and u is the cross-slope velocity. For the eddy streamfunction ψ^{eddy}, we take the along-shelf median instead of the mean because ψ^{eddy} is a noisy variable, as it is inversely proportional to (often large) vertical gradients of salinity and temperature (equation (3)).

Both components of the cross-slope overturning circulation (ψ^{mean} and ψ^{eddy}) tend to reinforce one another (as ST16 find in their idealized model) instead of cancelling out (Figures 4, S9, and S10), with the exceptions of the deeper half of the slope on the East Amundsen (Figure 4), Amery, and Central Weddell (Figures S9 and S10) segments. This result stands in contrast with the prevalent cancellation of Φ^{mean} and Φ^{eddy} both locally (Pearson's correlation coefficient $r = -0.97$ significant at the $\alpha = 99\%$ confidence level; Figures 3a and 3b) and in the segment-averaged sense (Table S1), which implies that there is some cancellation between the eddy advection ($\Phi^{\mathrm{eddy}}_{\mathrm{adv}}$; equation (2)) and eddy stirring ($\Phi^{\mathrm{eddy}}_{\mathrm{stir}}$) contributions to Φ^{eddy} along the 1,000-m isobath. The mean overturning circulation occupies the entire water column in all subsegments, and as a result, its sense determines the direction of Φ^{mean}: where ψ^{mean} is clockwise (negative; red shading in Figure 4f), warmer waters at depth (with higher CDW content) move upslope toward the shelf, while the cooler overlying waters (with higher AASW/Winter Water content) move offshore (Figures 4j–4l). Conversely, when the circulation is counterclockwise (positive; blue shading in Figures 4d and 4e), the opposite happens, and the net heat flux is offshore.

We now examine the advective ($\Phi^{\mathrm{eddy}}_{\mathrm{adv}}$) and stirring ($\Phi^{\mathrm{eddy}}_{\mathrm{stir}}$) contributions to Φ^{eddy} (Figures 4a–4c) in order to seek further insight into the processes responsible for eddy heat transfer and how they differ around the Antarctic continental margin. In the Oates subsegment, we find that onshore eddy thickness fluxes (positive $\Phi^{\mathrm{eddy}}_{\mathrm{adv}}$ and counterclockwise ψ^{eddy}; Figures 4a and 4g) transport heat from the CDW core at middepth away from the continental slope up to the ~2,000-m isobath, where isoneutral eddy stirring becomes dominant (positive $\Phi^{\mathrm{eddy}}_{\mathrm{stir}}$; Figure 4a), transferring heat all the way to the shelf edge (~500–1,000-m isobath), qualitatively consistent with ST16's along-shelf uniform simulation. In the East Ross, $\Phi^{\mathrm{eddy}}_{\mathrm{stir}}$ dominates the onshore Φ^{eddy} over the entire continental slope (Figure 4b), possibly as a result of the enhanced middepth cross-slope temperature gradient produced by the thin counterclockwise eddy overturning cell at the level of the CDW

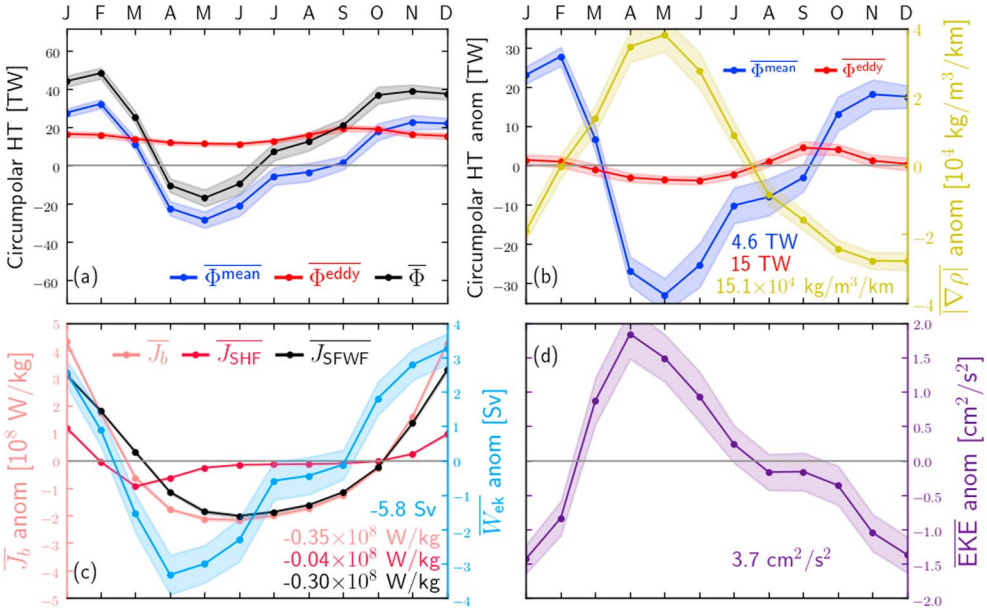

Figure 5. Climatological (1959–2009) seasonal cycle of circumpolarly integrated or averaged variables along the 1,000-m isobath (or area-averaged in case of the buoyancy fluxes). Quantities in (b)–(d) are monthly anomalies relative to the annual mean. (a) Monthly-averaged total ($\bar{\Phi}$), mean ($\overline{\Phi^{mean}}$), and eddy ($\overline{\Phi^{eddy}}$) circumpolar HTs across the 1,000-m isobath (magenta contour on the maps). (b) Circumpolarly and depth-averaged lateral density gradient magnitude ($\overline{|\nabla\rho|}$) and $\overline{\Phi^{mean}}$ and $\overline{\Phi^{eddy}}$. (c) Circumpolarly averaged Ekman transport divergence ($\overline{W_{ek}}$; positive when the net Ekman transport is more strongly offshore than in the climatological mean) and shelf-averaged net surface buoyancy flux ($\overline{J_b}$) and its surface heat ($\overline{J_{SHF}}$) and freshwater ($\overline{J_{SFWF}}$) flux components. The anomalies of the buoyancy fluxes are positive when the ocean gains more buoyancy than in the climatological mean). (d) Circumpolarly and depth-averaged Eddy Kinetic Energy ($\overline{EKE}$). The shaded envelopes indicate the 95% confidence intervals about each 1959–2009 climatology. The numbers on the lower-right corners are the mean values that were subtracted to produce the anomaly time series in (b)–(d). Note the amplitude of each variable's anomaly compared with its mean value (e.g., $\overline{J_b}$, $\overline{J_{SHF}}$, and $\overline{J_{SFWF}}$ change sign, while $\overline{W_{ek}}$ is negative year-round). HT = heat transport.

core (~500 m; Figures 4h and 4k). In the East Amundsen subsegment, the warm CDW tongue that penetrates far onto the shelf has a complicated overturning pattern (possibly because of its comparatively short along-shelf averaging length), and the on-shelf heat transport is accomplished mainly by a clockwise ψ^{mean}, with some reinforcement from the weakly clockwise ψ^{eddy} at the CDW level over the upper slope and outer shelf (Figures 4c, 4f, 4i, and 4l).

The remaining subsegments (Maud, Amery, West Ross, West Byrd, East Bellingshausen, and Central Weddell; Figures S9 and S10) feature both similarities and differences compared to the ones in Figure 4. The main similarities are that the direction of Φ^{mean} closely follows the sense of ψ^{mean} across the slope, that most of Φ^{eddy} and Φ^{mean} cancel out at all across-slope locations and the presence of intense clockwise ψ^{eddy} cells in the upper ~100 m (possibly the response of the mixed layer to the weather-band variability of the air-ice-ocean fluxes). However, note that equation (2) gives only an estimate of Φ^{eddy}_{adv} (and hence Φ^{eddy}_{stir}), as equation (3) itself is an asymptotic approximation to the eddy streamfunction in the Boussinesq case (see Stewart & Thompson, 2015a).

The full-depth character of ψ^{mean} is evident in all subsegments analyzed (Figures 4d–4f, S9, and S10). Combined with the approximate cancellation of the cross-slope mean heat transports within the near-surface and near-bottom layers (solid magenta and cyan lines in Figure 3c), this pattern indicates an approximately two-dimensional wind-driven mean circulation, with opposing Ekman transports within the top and bottom boundary layers, while the net heat transport is carried out by the eddies in the CDW layer within the geostrophic interior. This dynamical model is similar to that suggested by observational evidence from the Northwestern Weddell Sea (Thompson et al., 2014) and by ST16's numerical results, although our simulation's lower eddy kinetic energy levels underestimates ψ^{eddy} and Φ^{eddy}.

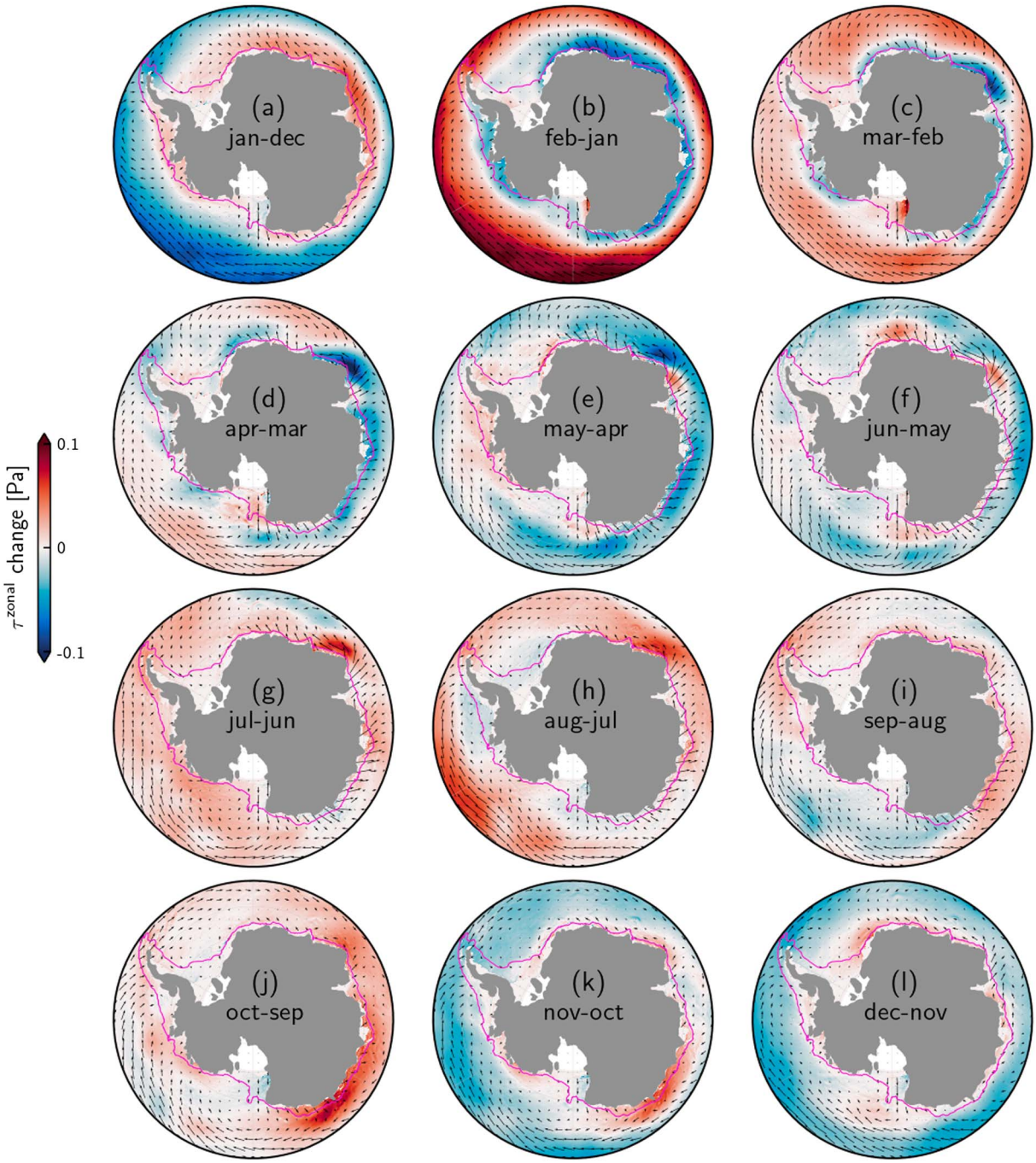

Figure 6. Climatological (1959–2009) seasonal cycle of the wind stress patterns over the Antarctic continental margin. Arrows are the monthly means of the wind stress vector, and the color shading is the difference in its zonal component relative to the previous month. For example, the shading in (a) represents the climatological January minus December zonal wind stress difference, while the arrows indicate the January climatological wind stress vector. Blue indicates strengthening of the easterlies and blocking of the onshore heat transport. Red indicates weakening of the easterlies and facilitation of the onshore heat transport. The magenta contour is the 1,000-m isobath.

5.2. The 1959–2009 Mean Seasonal Cycle

The seasonal cycles of the wind stress and the surface heat and buoyancy fluxes suggest that the lateral heat advection across and along isobaths may be coupled to these forcings. Indeed, the water mass structure has been observed to have strong seasonal variability in several segments of the ACS, including the regions off the Adélie Coast in East Antartica (Snow et al., 2016) and the Central Amundsen (Wåhlin et al., 2013), East Amundsen (Mallett et al., 2018), Ross (Castagno et al., 2017), and East Weddell (e.g., Ryan et al., 2017) Seas.

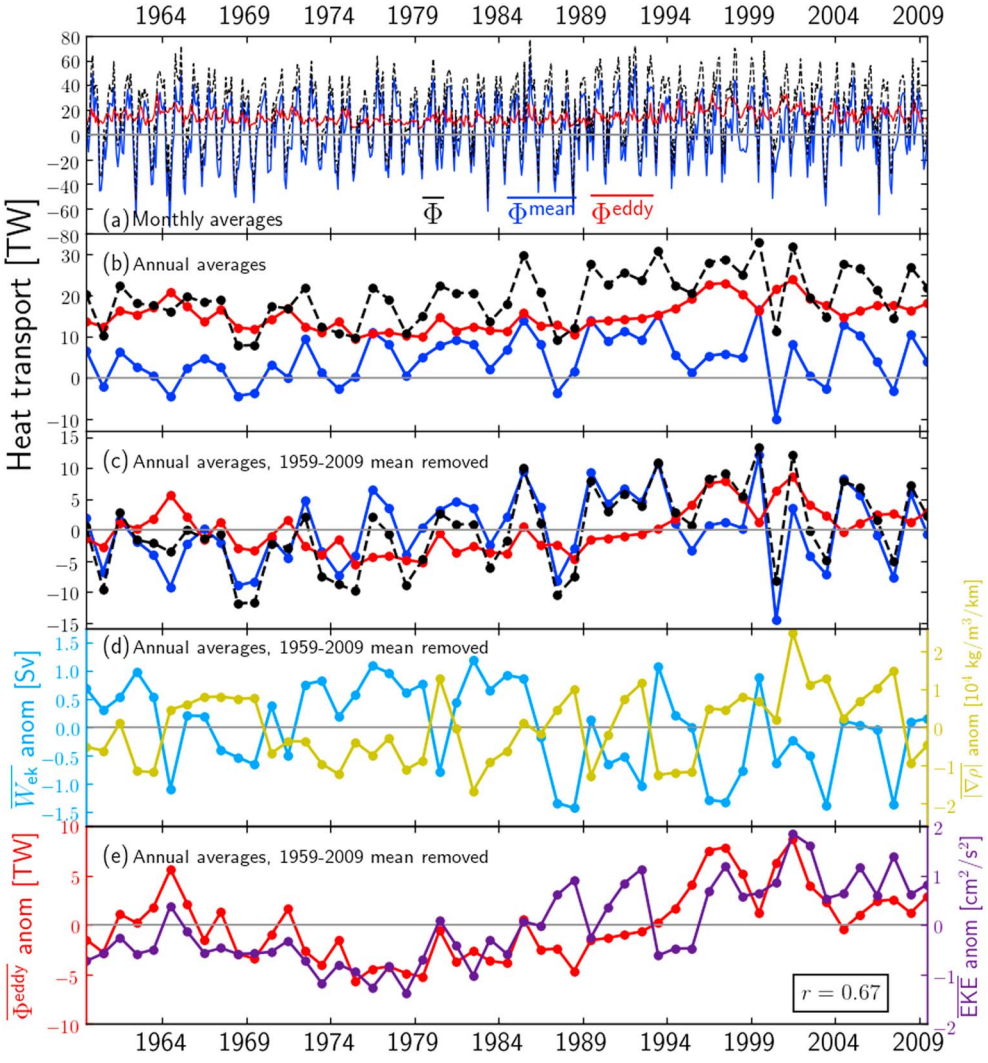

Figure 7. Interannual variability of the circumpolarly integrated heat transport across the 1,000-m isobath (positive onshore). (a) Time series of monthly averaged total ($\bar{\Phi}$), mean ($\overline{\Phi^{mean}}$), and eddy ($\overline{\Phi^{eddy}}$) heat transport. (b) Same as (a) but annually averaged. (c) Same as (b) but as anomalies relative to the long-term (1959–2009) mean. (d) Time series of annually averaged $\overline{W_{ek}}$ (blue) and $\overline{|\nabla\rho|}$ (yellow) as anomalies relative to the long-term (1959–2009) mean. (e) Time series of annually averaged $\overline{\Phi^{eddy}}$ and $\overline{EKE}$ as anomalies relative to the long-term (1959–2009) mean. The zero-lag correlation of 0.67 in (e) is significant at the 99.9% confidence level. EKE = Eddy Kinetic Energy.

With the exception of the Adélie Coast, these regions show a greater presence of warm CDW-influenced water on the shelf during summer and early fall. Can this variability be related to seasonality in the circumpolarly integrated on-shelf heat transport? We approach this question by examining the climatological eddy ($\overline{\Phi^{eddy}}$), mean ($\overline{\Phi^{mean}}$), and total ($\bar{\Phi}$) heat transport components (Figure 5a), and their anomalies relative to the annual mean (Figure 5b). Hereafter, all overbars ($\bar{\bullet}$) indicate circumpolarly integrated or averaged variables. Clearly, $\overline{\Phi^{mean}}$ (not $\overline{\Phi^{eddy}}$) dominates the seasonal variability of $\bar{\Phi}$ in the 1959–2009 mean seasonal cycle. This disparity is not as evident regarding the seasonality of the along-isobath averages of Φ^{mean} and Φ^{eddy} within each segment (Figure S3). $\bar{\Phi}$ ranges from −17 TW in May to 48 TW in February, which is approximately the same timing found by Dinniman et al. (2015, their Figure 12). At zero lag, $\overline{\Phi^{mean}}$ is positively correlated both with the circumpolar Ekman transport divergence ($\overline{W_{ek}}$; $r = 0.82$ significant at $\alpha = 99.9\%$) and surface buoyancy flux ($\overline{J_b}$; $r = 0.68$ at $\alpha = 99.9\%$). In contrast, $\overline{\Phi^{eddy}}$ correlates weakly with both variables at zero lag ($r = 0.03$ with $\overline{W_{ek}}$, not significant at $\alpha = 50\%$ and $r = 0.26$ with $\overline{J_b}$, significant at $\alpha = 99.9\%$). However, $\overline{\Phi^{eddy}}$ has maximum correlation at 5-month lag with $\overline{W_{ek}}$ ($r = -0.40$ significant at $\alpha = 99.9\%$) and at 7-month lag with $\overline{J_b}$ ($r = -0.61$ significant at $\alpha = 99.9\%$).

Although it is difficult to interpret the differences in the lags of maximum correlation between these quantities, the analyses above show that both wind and buoyancy forcings may have a causal link with $\bar{\Phi}$ and that $\overline{\Phi^{mean}}$ accounts for most of the variance in $\bar{\Phi}$. Is there a dominant forcing mechanism? Breaking $\overline{J_b}$ into its heat ($\overline{J_{SHF}}$) and freshwater ($\overline{J_{SFWF}}$) components reveals that $\overline{J_{SFWF}}$ is ~2–10 times larger than $\overline{J_{SHF}}$ (Figure 5c). During the sea ice formation season (March–September; Figure S2c), brine rejection and heat loss to the atmosphere (Figure 5c) diabatically decrease $\overline{|\nabla\rho|}$ and facilitate onshore heat transport. Conversely, when the sea ice is melting most rapidly (November–February; Figure S2c), $\overline{J_{SFWF}}$ and $\overline{J_b}$ (and to a lesser extent, $\overline{J_{SHF}}$) are most positive, helping increase $\overline{|\nabla\rho|}$ and hinder onshore $\bar{\Phi}$.

While the buoyancy forcing's contribution changes sign seasonally, $\overline{W_{ek}}$ is negative (i.e., convergent/downwelling-favorable) year-round (mean of −5.8 Sv) and therefore acts to block onshore $\bar{\Phi}$ on average. Over the summer (February–April), $\overline{W_{ek}}$ becomes incrementally more downwelling-favorable and that coincides with an increase in $\overline{|\nabla\rho|}$ and a decrease in $\bar{\Phi}$. The gradual increase in $\bar{\Phi}$ that follows (~May–February) correlates with the slackening of the downwelling-favorable $\overline{W_{ek}}$ and a decrease in both $\overline{|\nabla\rho|}$ and $\overline{EKE}$ (Figure 5).

These results suggest that the persistently downwelling-favorable mechanical forcing of the convergent Ekman transport overwhelms the steric contribution of the surface buoyancy fluxes controlled by the ocean-atmospere-sea ice interactions, therefore controlling the seasonal variability of $\overline{|\nabla\rho|}$, and hence $\overline{\Phi^{mean}}$ and $\bar{\Phi}$. This interpretation is supported by the climatological wind stress fields. From June through December/January, the easterlies weaken (especially in East Antarctica; red patches in Figure 6a and 6f–6l), while $\bar{\Phi}$ gradually increases onshore (Figures 5a and 5b). Later in the summer and into the fall (February–May), the easterlies quickly build up, increasing the onshore Ekman transport and strengthening the ASF (blue patches in Figures 6b–6e and 5b and 5c). This matches with the abrupt drop in $\bar{\Phi}$, which turns offshore in the fall (April–June). This interpretation is quantitatively supported by the stronger correlation of $\overline{\Phi^{mean}}$ with $\overline{W_{ek}}$ ($r = 0.82$, $\alpha = 99.9\%$) than with $\overline{J_b}$ ($r = 0.68$, $\alpha = 99.9\%$).

In accordance with the heat transport blocking paradigm (Spence et al., 2014), $\overline{EKE}$ and $\overline{|\nabla\rho|}$ are both 180° out of phase with $\overline{\Phi^{mean}}$ (Figures 5a, 5b, and 5d). However, $\overline{\Phi^{eddy}}$ has a very small seasonal amplitude (Figure 5b). This is perhaps surprising, since $\overline{EKE}$ has a well-defined seasonal signal, in phase with $\overline{|\nabla\rho|}$ ($r = 0.76$, significant at $\alpha = 99.9\%$; Figures 5b and 5d) as intuitively expected. Further, $\overline{\Phi^{eddy}}$ is very weakly correlated with $\overline{EKE}$ at zero lag ($r = 0.08$, significant at $\alpha = 85\%$). In order to satisfy the hypothesis that the circumpolar eddy heat transport responds to varying eddy activity of the ASC jet at monthly time scales, $\overline{EKE}$ and $\overline{\Phi^{eddy}}$ would need to be in phase and more strongly correlated. Still, $\overline{\Phi^{eddy}}$ has its maximum correlation with $\overline{EKE}$ at 5-month lag ($r = 0.46$, significant at $\alpha = 99.9\%$). Perhaps the local uplifting of isotherms associated with the arrival of remotely generated fast barotropic Kelvin waves (Spence et al., 2017) and/or slower continental shelf wave modes (Kusahara & Ohshima, 2009) can help explain this nonintuitive result. However, these processes are not identifiable in the present circumpolarly integrated, monthly averaged analysis.

5.3. Interannual Variability

5.3.1. Annually Averaged Circumpolar Heat Transport Time Series

In addition to seasonal changes in the continental shelf hydrography and circulation, the climate-scale wind forcing is known to drive significant variability in the transport of the ASC (e.g., Armitage et al., 2018; Stewart & Thompson, 2013). This can be expected to affect cross-isobath transports through the changes in the along-isobath pressure gradient force associated with the path of the ASC as it follows the continental slope and the more remote response of the shelf pressure field. The interannual variability of the time-mean and eddy components of the circumpolarly integrated heat transport across the 1,000-m isobath ($\overline{\Phi^{mean}}$ and $\overline{\Phi^{eddy}}$, respectively) is shown in Figures 7a–7c. Clearly, $\overline{\Phi^{mean}}$ is the major contributor to the variability of $\bar{\Phi}$, from monthly through interannual time scales. The monthly averaged $\overline{\Phi^{mean}}$ ranges from −75 to 62 TW, while $\overline{\Phi^{eddy}}$ ranges from 4 to 35 TW (Figure 7a). The annually averaged $\overline{\Phi^{mean}}$ ranges from −10 to 17 TW, while $\overline{\Phi^{eddy}}$ ranges from 9 to 24 TW. At time scales of 2–3 years, $\overline{\Phi^{mean}}$ varies more abruptly than $\overline{\Phi^{eddy}}$, which is seen also in the time series of $\overline{W_{ek}}$, $\overline{|\nabla\rho|}$, and $\overline{EKE}$ (Figures 7d and 7e). In some years, $\overline{\Phi^{mean}}$ even turns offshore, but $\overline{\Phi^{eddy}}$ is persistently onshore and therefore keeps the annually averaged $\bar{\Phi}$ positive (Figure 7b). The cumulative contribution of $\overline{\Phi^{eddy}}$ to the heat budget of the system in the 1959–2009 period is more than three times that of $\overline{\Phi^{mean}}$ (24 versus 7.2 YJ, not shown). Removing the individual 1959–2009 means from $\overline{\Phi^{mean}}$ and $\overline{\Phi^{eddy}}$ confirms that the time-mean background state plays a key role in the maintenance of a net on-shelf heat transport (Figure 7c).

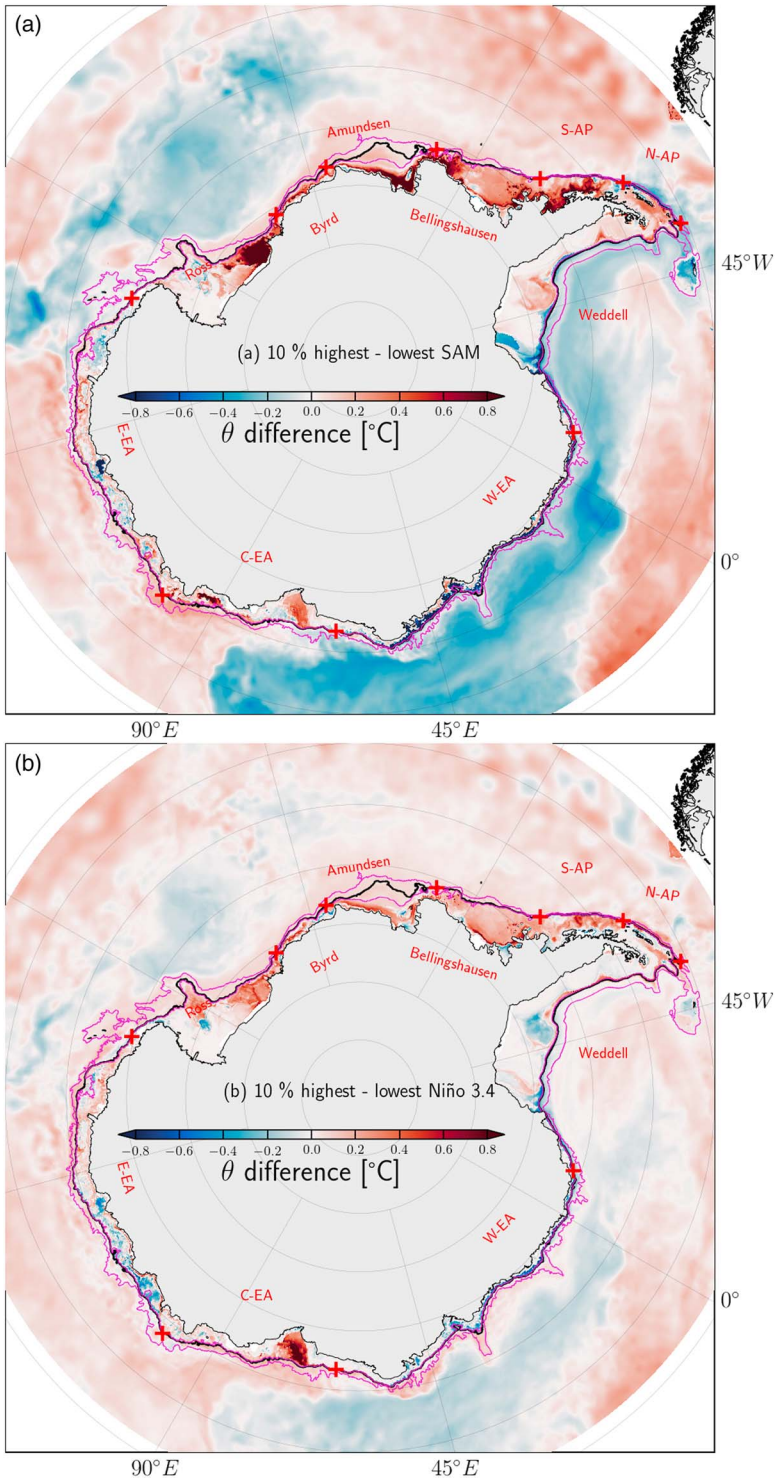

Figure 8. Spatial structure of the difference in the simulated potential temperature at 1,000 m or the bottom (whichever is shallower), conditionally averaged in high- and low-SAM years (a) and high- and low-Niño 3.4 years (b). The high-index and low-index composites are the averages of the years when either index is below its 10th percentile and above its 90th percentile, respectively. Red areas are warmer in high-SAM/high Niño 3.4 years compared to low-SAM/low Niño 3.4 years, while blue areas are colder. The magenta lines are the 800- and 2,500-m isobaths, and the black line is the 1,000-m isobath. Note the relative warming from the East Ross Sea to the tip of the Antarctic Peninsula, as well as some areas of East Antarctica for both SAM and Niño 3.4, although the differences associated with SAM are generally larger. SAM = Southern Annular Mode; S-AP = South Antarctic Peninsula; N-AP = North Antarctic Peninsula; E-EA = East portion of East Antarctica, C-EA = Central portion of East Antarctica; W-EA = West portion of East Antarctica.

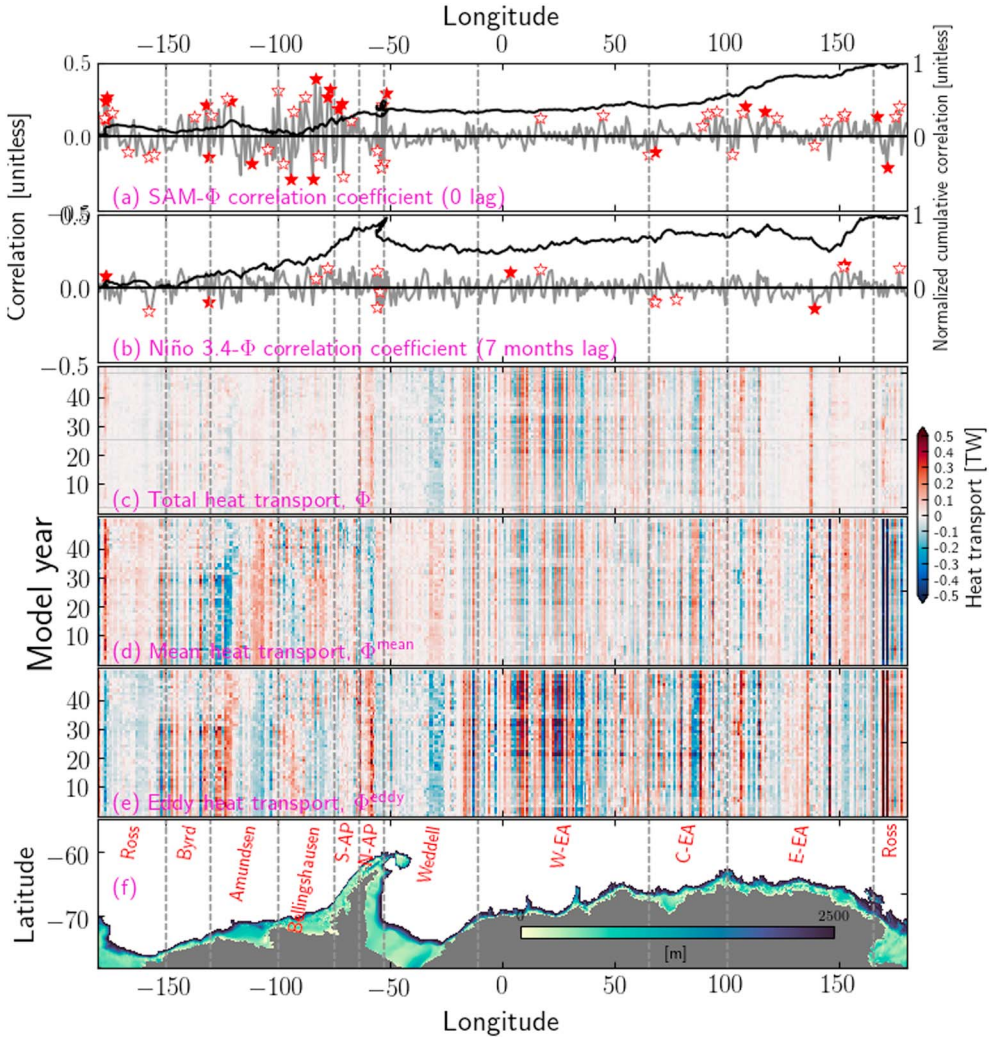

Figure 9. Temporal and spatial variability of the total (Φ), mean (Φ^{mean}), and eddy (Φ^{eddy}) cross-isobath heat transport. (a) Correlation coefficient at zero lag (gray line) and its along-isobath cumulative sum (black line) between Φ and the Southern Annular Mode (SAM) index as functions of distance along the 1,000-m isobath. (b) Same as (a) but for the Niño 3.4 index at 7-month lag. The filled and open stars in (a) and (b) indicate, respectively, points where the correlation is significant at the 95% and 80% confidence levels, accounting for the varying number of degrees of freedom at different along-isobath locations. (c–e) Annually averaged heat transports as functions of along-isobath distance and model year, averaged in 50-km-long along-isobath bins. (f) Reprise of Figure 3f. S-AP = South Antarctic Peninsula; N-AP = North Antarctic Peninsula; E-EA = East portion of East Antarctica, C-EA = Central portion of East Antarctica; W-EA = West portion of East Antarctica.

It is worth emphasizing that $\overline{\Phi^{eddy}}$ keeps $\bar{\Phi}$ positive both seasonally (Figure 5a) and interannually (Figure 7a). This result also holds regionally, as Φ^{mean} is either persistently offshore or turns offshore for several years in some segments, such as in E-EA and C-EA (containing Totten, Moscow University, and Amery Ice Shelves; Figure S5), while Φ^{eddy} is consistently onshore (albeit 5–10 times weaker in the segment-averaged sense; Figure S6). This reversal may cut off some ice shelves from or expose new ones to deep-ocean heat sources and thereby modulate their melt rates in segments where the along-shelf flow convergence does not compensate this heat deficit (Figure 3d). The common and sometimes persistent sign changes of Φ across segments support this conjecture (Figure S4). Interestingly, almost all of the along-shelf transport is due to the mean flow (not shown), in accord with SKM18's eddy-resolving modeling results. This suggests that eddies are not as important for along-shelf heat transport are they are for cross-shelf heat transport.

The relatively low intra-annual variance of $\overline{\Phi^{eddy}}$ compared to its mean counterpart (Figure S7) may be due to underestimated eddy kinetic energy in the present simulation (see section 2 and Figure 1d). Both the

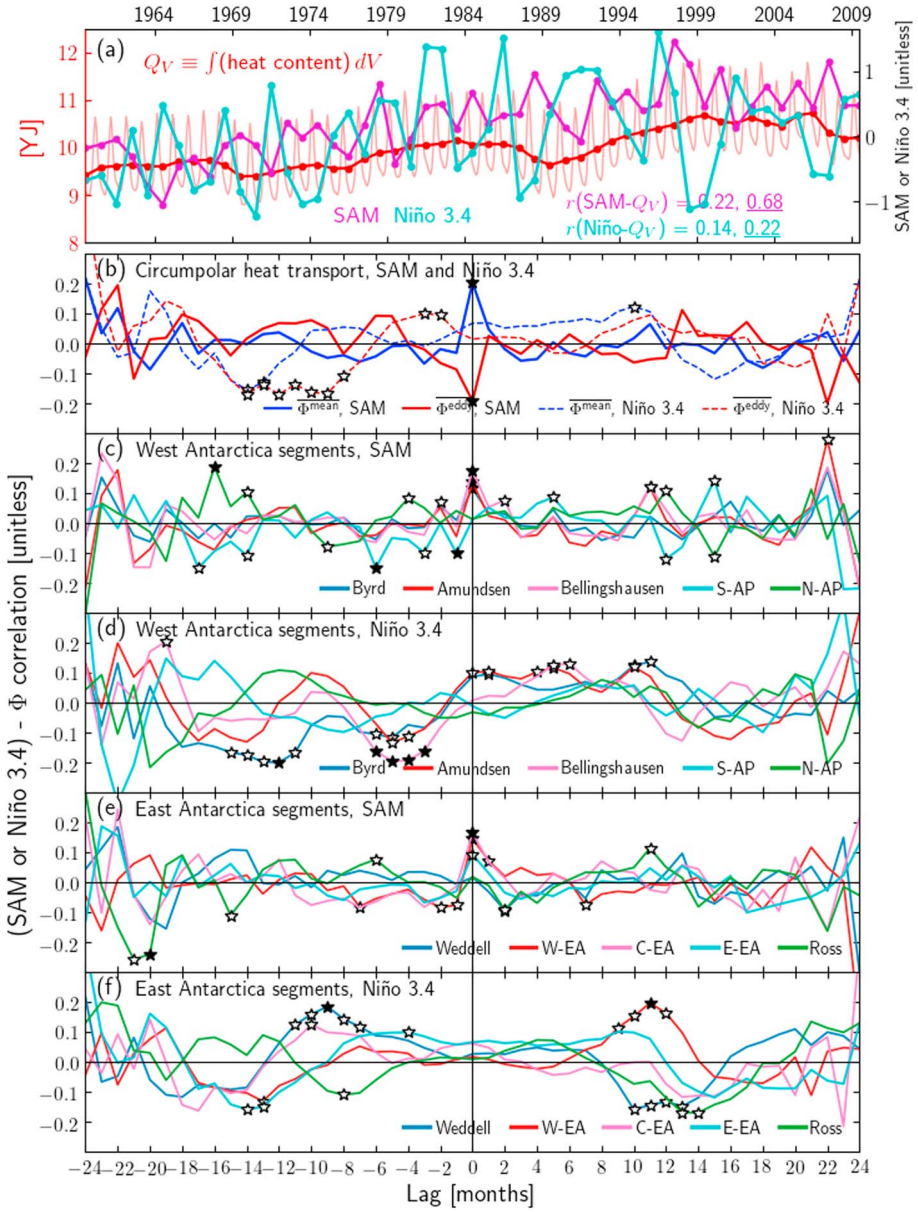

Figure 10. Circumpolar on-shelf heat transport and the Southern Annular Mode (SAM). (a) Circumpolar heat content Q_V (of the volume bounded by the 1,000-m isobath; Figure 1b), overlain with annual averages of SAM and Niño 3.4 indices. The faint red line is the monthly averaged Q_V, while the heavy red line is the annually averaged Q_V. The Q_V-SAM and Q_V- Niño 3.4 zero-lag correlation coefficients are shown both for the monthly and annually averaged time series, with the annually averaged values underlined. For SAM, the monthly mean and the annual mean correlations with Q_V are both significant at the 99.9% confidence level, while the Q_V- Niño 3.4 correlations are significant at the 99.0% (monthly) and 80% (annual) confidence levels. (b) Lagged correlation coefficient between either SAM or Niño 3.4 and the circumpolarly integrated mean ($\overline{\Phi^{mean}}$) and eddy ($\overline{\Phi^{eddy}}$) on-shelf heat transports. (c and d) Lagged correlation coefficient between either SAM (c) or Niño 3.4 (d) and the along-isobath averages of Φ for the Western segments. (e and f) Same as (c) and (d) but for the Eastern segments. The filled and open stars in (b)–(f) indicate, respectively, correlations that are significant at the 95% and 80% confidence levels, accounting for the varying number of degrees of freedom for different segments and at different lags. S-AP = South Antarctic Peninsula; N-AP = North Antarctic Peninsula; E-EA = East portion of East Antarctica, C-EA = Central portion of East Antarctica; W-EA = West portion of East Antarctica.

spatial distribution and the magnitude of $\overline{\Phi^{eddy}}$ are known to be sensitive to model grid resolution (Graham et al., 2016; Stewart & Thompson, 2015b; SKM18). Hence, we expect a finer-resolution POP/CICE simulation (currently in production) to have different magnitudes and patterns of EKE and Φ^{eddy}. Like in SKM18, the time-mean EKE in our simulation is evenly distributed over most of the continental slope and shelf and is elevated only at a few locations such as the central Weddell and Ross Seas (Figure 1d).

5.3.2. Relation to Climate Modes

Wind perturbations in East Antarctica are known to produce both local and remote changes in the heat content at the edge of the continental shelf through modulation of the ASF, often linked to the SAM (Stewart & Thompson, 2013; Spence et al., 2017). Likewise, El Niño events have been shown to impact the mass balance of ice shelves in West Antarctica through the competition between increased snowfall (thickening) being offset by enhanced basal melt rates (thinning; Paolo et al., 2018). We now examine a possible causal relationship between these climate modes and the interannual variability of the heat transports described in the previous section.

Figure 8a shows the difference in potential temperature at 1,000 m or the bottom (whichever is shallower locally) between a conditionally averaged high-SAM scenario (average of years when the SAM index exceeds the 90th percentile) and a low-SAM scenario (average of years when the SAM index is below the 10th percentile). Warming of typically 0.5–1 °C is found in the East Ross, East Amundsen, and West Bellingshausen Seas and in the C-EA segment (off the Amery Ice Shelf location, ~ 75° E), while cooling of a similar magnitude is found in the W-EA segment, in parts of the E-EA segment, and in the East Weddell Sea (Filchner Trough, ~30° W). Figure 8b plots the same type of potential temperature difference but for the Niño 3.4 index. The warming relative to low-Niño 3.4 years covers a similar but slightly larger area than the SAM case, although the magnitudes of the difference are smaller in the Niño 3.4 case. The regions where there is a higher warming than in the SAM case are off of the Amery Ice Shelf and Filchner Trough.

This spatially (i.e., along-isobath) heterogeneous temperature response to the SAM-related poleward shift of the easterlies is consistent with the spatial structure of the zero-lag correlation between Φ and the SAM index. The SAM and Niño 3.4 indices have maximum correlation with $\bar{\Phi}$ at zero lag and 7–9-month lag, respectively (not shown), and we therefore examine the along-isobath structure of the correlations at these lags in Figure 9. The SAM-Φ correlations change over short along-isobath distances but are generally positive over most of East Antarctica, West Amundsen, and East Bellingshausen Seas (Figure 9a). The Niño 3.4-Φ correlations are generally weaker but more consistently positive in West Antarctica than the SAM-Φ correlations (Figure 9b). Also, Figures 9c–9e show that the local cancellation patterns between Φ^{mean} and Φ^{eddy} found in Figure 3a, 3b, and 3d are persistent throughout the 1959–2009 span of the simulation over virtually the entire Antarctic continental margin, as a result of the ubiquitous recirculation along the shelf edge.

Despite the mean/eddy cancellation, the heat content of the Antarctic continental shelf, Q_V (defined as the volume enclosed by the 1,000-m isobath; magenta line on Figure 8), is positively correlated with the SAM index in the annually averaged sense ($r = 0.68$ significant at $\alpha = 99.9\%$), while the Niño 3.4 index is not (Figure 10a). The circumpolar integrals of the on-shelf heat transport components ($\overline{\Phi^{mean}}$ and $\overline{\Phi^{eddy}}$) are weakly but significantly correlated with the SAM index at zero lag ($r \sim 0.2$ and $r \sim -0.2$, respectively, both significant at $\alpha = 95\%$; Figure 10b). Within individual segments, the along-isobath averages of Φ are also significantly correlated with SAM at zero lag at the Byrd, Amundsen, and Bellingshausen segments in West Antarctica (Figure 10c) and across all of East Antarctica (segments W-EA, C-EA, and E-EA; Figure 10e). These results suggest that the SAM, possibly via its modulation of the ASF structure (Armitage et al., 2018), is more important than ENSO as a climate driver of onshore heat transport at the circumpolar scale.

What are the physical mechanisms linking the simulated SAM variability to the cross-isobath heat transport? In sections 5.2 and 5.3, we used the conceptual model of Spence et al. (2014) to explain the seasonal and interannual variabilities of $\bar{\Phi}$ as a response to the cross-shelf downwelling circulation forced by circumpolar Ekman transport convergence. The markedly circumpolarly symmetric pattern of negative correlation between the SAM index and the coastal sea level anomaly at zero lag, combined with the lack of correlation at larger lags (Armitage et al., 2018, their Figure S7) supports this interpretation. We find the highest correlation between the circumpolar Ekman transport divergence ($\overline{W_{ek}}$) and SAM at zero lag, while the highest correlation between $\overline{W_{ek}}$ and Niño 3.4 is at 10-month lag (not shown). This implies that stronger simulated SAM events are indeed related to weakened easterlies (or strengthened westerlies) and decreased onshore Ekman transport and downwelling (or enhanced offshore Ekman transport and upwelling) at the circumpolar scale. This would

produce a negative correlation between the SAM index and the coastal sea level anomaly, which is consistent with observations (Armitage et al., 2018). Since the observed SAM index typically decorrelates in less than 6 months (Armitage et al., 2018, their Figure S8) as well as in CORE-II (integral time scale of 1.1 months, not shown), it is not surprising that higher correlations are not found at lags larger than about a year.

The Niño 3.4 index contrasts with the SAM, in that it has no strong correlation with any of the circumpolar variables (Q_V, $\overline{\Phi^{mean}}$ or $\overline{\Phi^{eddy}}$) at zero lag (Figures 10a and 10b). Weak correlations ($r \sim 0.1$, significant at $\alpha = 80\%$) with $\overline{\Phi^{mean}}$ and $\overline{\Phi^{eddy}}$ exist at 10–12 month lag (Figure 10b), which can be traced to significant correlations with the segment-averaged Φ in the Amundsen and Bellingshausen segments (Figure 10d), supporting the causal link between ENSO and ocean variability in West Antarctica found in previous studies (e.g., Paolo et al., 2018; Steig et al., 2012). These correlations are consistent with the hypothesis that the SAM is a more significant climate driver for on-shelf transport of warm CDW than ENSO, particularly in East Antarctica (Figure 10a).

In West Antarctica, episodic warm intrusions found in global simulations have been connected to the arrival of fast, barotropic Kelvin waves originating from wind perturbations in East Antarctica (Spence et al., 2017). Our findings suggest that a similar mechanism may be operating in POP: monthly time scale changes in the zonal wind along East Antarctica (exemplified by the localized seasonal patches in Figure 6) serve as an ancillary mechanism for warm intrusions along the shelf edge in West Antarctica. However, it is unclear whether the feedbacks of this increased onshore heat transport with other regional changes induced by climate modes (e.g., circulation and/or heat content changes due to modified meltwater input or surface heat flux) would result in a net increase or decrease of heat actually reaching the ice shelves.

6. Summary and Conclusions

In this study, we have analyzed some of the large-scale, low-frequency physical processes involved in the onshore transport of heat across the ACS, based on fields from a 0.1°-resolution global coupled ocean-sea ice model (POP2/CICE4) forced by realistic, interannually varying atmospheric forcing. This 50-year (1959–2009) subset of the model output has enabled us to analyze the cross-ACS heat transport throughout all Antarctic marginal seas over time scales ranging from seasonal to multidecadal. We examined the vertical water mass structure along the simulated ACS by comparing temporally and spatially averaged simulated Conservative Temperature (Θ) and Absolute Salinity (S_A) profiles with observations from the MEoP data set (Figure 2), which indicated good representation of the time-averaged ACS stratification by the model. Agreement of the simulated heat transport magnitudes and along-isobath scales with those reported in independent studies (Graham et al., 2016; Rodriguez et al., 2016; Table 1) is also found. The 50-year (1959–2009) averages of the vertically integrated mean (Φ^{mean}) and eddy (Φ^{eddy}) cross-slope heat transports along the 1,000-m isobath show important areas of convergence of the along-shelf heat transport and the existence of O(100–1,000 km) segments of persistent cross-isobath heat transport (Figure 3). Analysis of the cross-shelf structure of the mean and eddy overturning circulations in different segments of the ACS (Figures 4, S9, and S10) revealed that advection due to the mean flow or eddies and stirring of potential temperature along density surfaces by eddies can operate in different combinations depending on the isobath and the along-shelf location. In the climatological annual cycle, Φ^{mean} (representing monthly mean heat transport) dominates, while Φ^{eddy} (representing effects due to anomalies relative to the monthly mean) is relatively constant throughout the year (Figure 5). November-February peaks and April-June troughs in heat transport are consistent with a response to seasonal wind variability in the Southern Ocean (Figure 6). On longer time scales (Figure 7), some of the variability of the heat transport correlates with changes in the SAM and the ENSO (Figures 8, 9, and 10). In brief, our main conclusions are

1. The 0.1° POP2/CICE4 simulation has a realistic time-mean stratification in the pycnocline layer along the Antarctic margin but has biases at the core depth of O(10–100 m) and the core temperature (typically 0.1–0.5 °C) of the CDW;
2. The ranges of annually averaged circumpolar integrals of the mean ($\overline{\Phi^{mean}}$), eddy ($\overline{\Phi^{eddy}}$), and total ($\bar{\Phi}$) on-shelf heat transport are −10–17 TW, 9–24 TW, and 8–33 TW, respectively;
3. As functions of the along-isobath distance y, both the time-mean $\Phi^{mean}(y)$ and the eddy $\Phi^{eddy}(y)$ components of the heat transport have coherent spatial structures at scales of O(100–1,000 km), and they partially cancel locally;
4. Eddy stirring of potential temperature along isoneutral surfaces (Φ^{eddy}_{stir}) seems to be the dominant form of eddy heat transport (both onshore and offshore) in most segments, supporting previous findings (ST16; SKM18);

5. Where Φ^{eddy} is offshore, Φ^{mean} is onshore, associated with a full-depth, clockwise cross-isobath overturning circulation moving warm CDW-influenced water onshore and overlying AASW/WW offshore;
6. Seasonal variability of $\bar{\Phi}$ is dominated by $\overline{\Phi^{mean}}$;
7. The variability of the total circumpolar convergence of the cross-isobath surface Ekman transport is a stronger driver of $\overline{\Phi^{mean}}$ (and hence $\bar{\Phi}$) than the circumpolar surface buoyancy flux; and
8. Interannual and longer-period variability of $\bar{\Phi}$ can be interpreted as a response to the zonally symmetric wind stress variability linked to the SAM and a smaller contribution from El Niño events, whose influence is more prevalent in West Antarctica.

This study has some limitations and caveats. Our 0.1° POP2/CICE4 simulation's resolution only partially resolves eddies on the ACS and shelf and has no ice shelves or continental freshwater release and no tidal forcing. Recent results demonstrate the important roles of these forcings in the cross-ACS heat transport. We also expect the choice of a fixed isobath as the boundary of the coastal control volume to introduce some bias in the heat transport calculations, because it does not always record the heat transport across the moving ASF axis (as discussed by Goddard et al., 2017, for their simulation).

For most of the Antarctic margin, the emerging picture for the coastal circulation seems to confirm the paradigm proposed by Dinniman and Klinck (2004): the cross-slope heat transport is driven partially by mean flow-topography interaction processes such as inertial overshooting of the ASC, but the shelf circulation must conspire to enable the heat originating from the ACC to actually reach the ice shelves instead of recirculating back offshore. In this regard, an encouraging aspect of our time-averaged analyses is the existence of O(1 TW) heat transports locked to sharp topographic features (Figure 3a–3c and 3f), as found in eddy-permitting (4 km) and eddy-resolving (1.5 km) simulations (Graham et al., 2016; St-Laurent et al., 2013, Figure 7 in the latter) and observations (e.g., Walker et al., 2007; Wåhlin et al., 2013). Despite the underrepresentation of eddies, our modeling results suggest that barotropic mean flow-topography interaction processes may be locally important, as found by Goddard et al. (2017) in their simulation and by Kalén et al. (2015) in their observations of flow in the Dotson Trough in the Amundsen Sea.

Considering the interannual and decadal trends in Θ and S_A estimated by Schmidtko et al. (2014), the deep ocean is likely to be a major driver of changes in the cross-ACS heat transport at the circumpolar scale, although there does not seem to be a single process or even a relatively broadly applicable combination of processes able to account for all of the oceanic heat entering the Antarctic shelf. The cross-ACS heat transport may be modified by changes in the stratification of the ASC/ASUC system or the ACC (through thermal wind shear, e.g., Chavanne et al., 2010; Martinson & McKee, 2012; Walker et al., 2007, 2013) by a poleward migration of the Southern ACC front, or by an increase in the cross-ACC eddy heat transport. At present, a robust change in the zonally averaged latitude of the ACC has not been observed (Gille et al., 2016), although a more localized incursion of its southern front (e.g., Figure S8) could also be capable of delivering heat to previously sheltered ice shelves in key regions. The large-scale shoaling and deepening trends in the CDW core along the ACS and their correlation with the temperature trends at the bottom of the adjacent shelf (Schmidtko et al., 2014, their Figure 2) can perhaps be explained by a combination of these processes.

In conclusion, response to large-scale differences in surface buoyancy and wind forcing, bottom topography, and the continental shelf circulation is probably important in different combinations in each marginal sea, although the availability of warm CDW at the shelf edge (modulated by the ASC/ASUC and ACC) is ultimately necessary to support the simulated and observed heat transports at very low frequencies. Locally, the amount of oceanic heat actually reaching the subglacial cavities is likely to be more strongly constrained by a complex combination of bottom topography, surface buoyancy fluxes, and the convergence/divergence of along-shelf temperature advection, rather than the cross-isobath heat transport alone. Examination of the combined effects of these forcings and their interactions with the low-frequency cross-shelf heat transports examined in this study awaits longer eddy-resolving model simulations with tides, freshwater fluxes, and thermodynamically active ice-shelf cavities.

Acknowledgments
The authors gratefully acknowledge support from the US Department of Energy (DOE, grant DE-SC0014440) in the scope of the "Ocean and Sea Ice and their Interactions around Greenland and the West Antarctic Peninsula in Forced Fine-Resolution Global Simulations" project and high-performance computing support from Yellowstone (ark:/85065/d7wd3xhc) provided by NCAR's Climate Simulation Laboratory (CSL), sponsored by the National Science Foundation (NSF) and other agencies. J. L. M. was supported by an earlier U.S. DOE Office of Science grant entitled "Ultra-High Resolution Global Climate Simulation" via a Los Alamos National Laboratory subcontract to carry out the POP/CICE simulation; both Caroline Papadopoulos (SIO/UCSD) and Elena Yulaeva (UCSD) participated in its production. The analyses of the model output performed in this study were enabled by computing resources provided by Oak Ridge Leadership Computing Facility (OLCF). The marine mammal data were collected and made freely available by the International MEoP Consortium and the national programs that contribute to it (http://www.meop.net). All code and reduced data sets necessary to reproduce the results are available online at https://github.com/apaloczy/AntarcticaCircumpolarIntrusions. We are grateful to two anonymous reviewers, whose thorough work substantially improved the quality of the manuscript.

References

Armitage, T. W. K., Kwok, R., Thompson, A. F., & Cunningham, G. (2018). Dynamic topography and sea level anomalies of the Southern Ocean: Variability and teleconnections. *Journal of Geophysical Research: Oceans*, *123*, 613–630. https://doi.org/10.1002/2017JC013534

Assmann, K. M., Jenkins, A., Shoosmith, D. R., Walker, D. P., Jacobs, S. S., & Nicholls, K. W. (2013). Variability of circumpolar deep water transport onto the Amundsen Sea Continental shelf through a shelf break trough. *Journal of Geophysical Research: Oceans*, *118*, 6603–6620. https://doi.org/10.1002/2013JC008871

Castagno, P., Falco, P., Dinniman, M. S., Spezie, G., & Budillon, G. (2017). Temporal variability of the circumpolar deep water inflow onto the Ross Sea continental shelf. *Journal of Marine Systems*, *166*, 37–49. https://doi.org/10.1016/j.jmarsys.2016.05.006

Cavalieri, D. J., Gloersen, P., & Campbell, W. J. (1997). Determination of sea ice parameters with the NIMBUS 7 SMMR. *Journal of Geophysical Research*, *89*(D4), 5355–5369. https://doi.org/10.1029/JD089iD04p05355

Chavanne, C. P., Heywood, K. J., Nicholls, K. W., & Fer, I. (2010). Observations of the Antarctic slope undercurrent in the southeastern Weddell Sea. *Geophysical Research Letters*, *37*, L13601. https://doi.org/10.1029/2010GL043603

Cook, A. J., Holland, P. R., Meredith, M. P., Murray, T., Luckman, A., & Vaughan, D. G. (2016). Ocean forcing of glacier retreat in the western Antarctic Peninsula. *Science*, *353*(6296), 283–286. https://doi.org/10.1126/science.aae0017

Couto, N., Martinson, D. G., Kohut, J., & Schofield, O. (2017). Distribution of upper circumpolar deep water on the warming continental shelf of the West Antarctic Peninsula. *Journal of Geophysical Research: Oceans*, *122*, 5306–5315. https://doi.org/10.1002/2017JC012840

Dinniman, M., Asay-Davis, X., Galton-Fenzi, B., Holland, P., Jenkins, A., & Timmermann, R. (2016). Modeling ice shelf/ocean interaction in Antarctica: A review. *Oceanography*, *29*(4), 144–153. https://doi.org/10.5670/oceanog.2016.106

Dinniman, M. S., & Klinck, J. M. (2004). A model study of circulation and cross-shelf exchange on the west Antarctic Peninsula continental shelf. *Deep-Sea Research Part II: Topical Studies in Oceanography*, *51*(17-19), 2003–2022. https://doi.org/10.1016/j.dsr2.2004.07.030

Dinniman, M. S., Klinck, J. M., Bai, L. S., Bromwich, D. H., Hines, K. M., & Holland, D. M. (2015). The effect of atmospheric forcing resolution on delivery of ocean heat to the Antarctic floating ice shelves. *Journal of Climate*, *28*(15), 6067–6085. https://doi.org/10.1175/JCLI-D-14-00374.1

Dinniman, M. S., Klinck, J. M., & Smith, W. O. (2011). A model study of circumpolar deep water on the west Antarctic Peninsula and Ross Sea continental shelves. *Deep-Sea Research Part II: Topical Studies in Oceanography*, *58*, 1508–1523. https://doi.org/10.1016/j.dsr2.2010.11.013

Downes, S. M., Farneti, R., Uotila, P., Griffies, S. M., Marsland, S. J., Bailey, D., et al. (2015). An assessment of Southern Ocean water masses and sea ice during 1988-2007 in a suite of interannual CORE-II simulations. *Ocean Modelling*, *94*, 67–94. https://doi.org/10.1016/j.ocemod.2015.07.022

Fogt, R. L., Bromwich, D. H., & Hines, K. M. (2011). Understanding the SAM influence on the South Pacific ENSO teleconnection. *Climate Dynamics*, *36*(7–8), 1555–1576. https://doi.org/10.1007/s00382-010-0905-0

Gent, P. R., & McWilliams, J. C. (1990). Isopycnal mixing in ocean circulation models. *Journal of Physical Oceanography*, *20*(1), 150–155. https://doi.org/10.1175/1520-0485(1990)020<0150:IMIOCM>2.0.CO;2

Gille, S. T., McKee, D. C., & Martinson, D. G. (2016). Temporal changes in the Antarctic circumpolar current: Implications for the Antarctic continental shelves. *Oceanography*, *29*, 96–105. https://doi.org/10.5670/oceanog.2016.102

Goddard, P. B., Dufour, C. O., Yin, J., Griffies, S. M., & Winton, M. (2017). CO_2-induced ocean warming of the Antarctic continental shelf in an eddying global climate model. *Journal of Geophysical Research: Oceans*, *122*, 8079–8101. https://doi.org/10.1002/2017JC012849

Graham, J. A., Dinniman, M. S., & Klinck, J. M. (2016). Impact of model resolution for on-shelf heat transport along the West Antarctic Peninsula. *Journal of Geophysical Research: Oceans*, *121*, 7880–7897. https://doi.org/10.1002/2016JC011875

Greenbaum, J. S., Blankenship, D. D., Young, D. A., Richter, T. G., Roberts, J. L., Aitken, A. R. A., et al. (2015). Ocean access to a cavity beneath Totten Glacier in East Antarctica. *Nature Geoscience*, *8*(4), 294–298. https://doi.org/10.1038/ngeo2388

Gunn, K. L., White, N. J., Larter, R. D., & Caulfield, C. P. (2018). Calibrated seismic imaging of eddy-dominated warm-water transport across the Bellingshausen Sea, Southern Ocean. *Journal of Geophysical Research: Oceans*, *123*, 3072–3099. https://doi.org/10.1029/2018JC013833

Ha, H. K., Wåhlin, A. K., Kim, T. W., Lee, S. H., Lee, J. H., Lee, H. J., et al. (2014). Circulation and modification of warm deep water on the central Amundsen shelf. *Journal of Physical Oceanography*, *44*(5), 1493–1501. https://doi.org/10.1175/JPO-D-13-0240.1

Hammond, M. D., & Jones, D. C. (2016). Freshwater flux from ice sheet melting and iceberg calving in the Southern Ocean. *Geoscience Data Journal*, *3*(2), 60–62. https://doi.org/10.1002/gdj3.43

Hunke, E. C., Lipscomb, W. H., Turner, A. K., Jeffery, N., & Elliott, S. (2010). CICE: The Los Alamos sea ice model documentation and software user's manual version 4.1 LA-CC-06-012 (Tech. rep.). Los Alamos, NM: T-3 Fluid Dynamics Group Los Alamos National Laboratory.

Jenkins, A., Dutrieux, P., Jacobs, S., Steig, E. J., Gudmundsson, G. H., & Smith, J. (2016). Decadal ocean forcing and Antarctic ice sheet response: Lessons from the Amundsen Sea. *Oceanography*, *29*(4), 106–117. https://doi.org/https://doi.org/10.5670/oceanog.2016.103

Jourdain, N. C., Mathiot, P., Merino, N., Durand, G., Le Sommer, J., Spence, P., et al. (2017). Ocean circulation and sea-ice thinning induced by melting ice shelves in the Amundsen Sea. *Journal of Geophysical Research: Oceans*, *122*, 2550–2573. https://doi.org/10.1002/2016JC012509

Kalén, O., Assmann, K. M., Wåo hlin, A. K., Ha, H. K., Kim, T. W., & Lee, S. H. (2015). Is the oceanic heat flux on the central Amundsen Sea shelf caused by barotropic or baroclinic currents? *Deep-Sea Research Part II: Topical Studies in Oceanography*, *123*, 7–15. https://doi.org/10.1016/j.dsr2.2015.07.014

Kusahara, K., & Ohshima, K. I. (2009). Dynamics of the wind-driven sea level variation around Antarctica. *Journal of Physical Oceanography*, *39*(3), 658–674. https://doi.org/10.1175/2008JPO3982.1

Kusahara, K., & Ohshima, K. I. (2014). Kelvin waves around Antarctica. *Journal of Physical Oceanography*, *44*(11), 2909–2920. https://doi.org/10.1175/JPO-D-14-0051.1

Large, W. G., McWilliams, J. C., & Doney, S. C. (1994). Oceanic vertical mixing: A review and a model with a nonlocal boundary layer parameterization. *Reviews of Geophysics*, *32*(4), 363–403. https://doi.org/10.1029/94RG01872

Large, W. G., & Yeager, S. G. (2009). The global climatology of an interannually varying air–sea flux data set. *Climate Dynamics*, *33*(2), 341–364. https://doi.org/10.1007/s00382-008-0441-3

Liu, Y., Moore, J. C., Cheng, X., Gladstone, R. M., Bassis, J. N., Liu, H., et al. (2015). Ocean-driven thinning enhances iceberg calving and retreat of Antarctic ice shelves. *Proceedings of the National Academy of Sciences*, *112*(11), 3263–3268. https://doi.org/10.1073/pnas.1415137112

Mallett, H. K. W., Boehme, L., Fedak, M., Heywood, K. J., Stevens, D. P., & Roquet, F. (2018). Variation in the distribution and properties of circumpolar deep water in the eastern Amundsen Sea, on seasonal timescales, using seal-borne tags. *Geophysical Research Letters*, *45*, 4982–4990. https://doi.org/10.1029/2018GL077430

Martinson, D. G., & McKee, D. C. (2012). Transport of warm upper circumpolar deep water onto the western Antarctic Peninsula continental shelf. *Ocean Science*, *8*(4), 433–442. https://doi.org/10.5194/os-8-433-2012

Martinson, D. G., Stammerjohn, S. E., Iannuzzi, R. A., Smith, R. C., & Vernet, M. (2008). Western Antarctic Peninsula physical oceanography and spatio-temporal. *Deep-Sea Research Part II: Topical Studies in Oceanography*, *55*(18-19), 1964–1987. https://doi.org/10.1016/j.dsr2.2008.04.038

McClean, J. L., Bader, D. C., Maltrud, M. E., Evans, K. J., Taylor, M., Tang, Q., et al. (2018). High-resolution fully-coupled ACME v0.1 approximate present day transient climate simulations, Ocean Sciences Meeting 2018, 12–16/February, Portland/OR. Abstract ID: OM44C-2143.

Moffat, C., Owens, B., & Beardsley, R. C. (2009). On the characteristics of circumpolar deep water intrusions to the west Antarctic Peninsula continental shelf. *Journal of Geophysical Research*, *114*, C05017. https://doi.org/10.1029/2008JC004955

Nakayama, Y., Schröder, M., & Hellmer, H. H. (2013). From circumpolar deep water to the glacial meltwater plume on the eastern Amundsen Shelf. *Deep-Sea Research Part I: Oceanographic Research Papers*, *77*, 50–62. https://doi.org/10.1016/j.dsr.2013.04.001

Nerem, R. S., Beckley, B. D., Fasullo, J. T., Hamlington, B. D., Masters, D., & Mitchum, G. T. (2018). Climate-change-driven accelerated sea-level rise detected in the altimeter era. *Proceedings of the National Academy of Sciences*, *115*(9), 2022–2025. https://doi.org/10.1073/pnas.1717312115

Nøst, O. A., Biuw, M., Tverberg, V., Lydersen, C., Hattermann, T., Zhou, Q., et al. (2011). Eddy overturning of the Antarctic Slope Front controls glacial melting in the eastern Weddell Sea. *Journal of Geophysical Research*, *116*, C11014. https://doi.org/10.1029/2011JC006965

Pacanowski, R. C., & Gnanadesikan, A. (1998). Transient response in a Z-level ocean model that resolves topography with partial cells. *Monthly Weather Review*, *126*(12), 3248–3270.

Paolo, F. S., Fricker, H. A., & Padman, L. (2015). Volume loss from Antarctic ice shelves is accelerating. *Science*, *348*(6232), 327–331.

Paolo, F. S., Padman, L., Fricker, H. A., Adusumilli, S., Howard, S., & Siegfried, M. R. (2018). Response of Pacific-sector Antarctic ice shelves to the El Niño/Southern oscillation. *Nature Geoscience*, *11*(February), 121–126. https://doi.org/10.1038/s41561-017-0033-0

Peña-Molino, B., McCartney, M. S., & Rintoul, S. R. (2016). Direct observations of the Antarctic slope current transport at 113°. *Journal of Geophysical Research: Oceans*, *121*, 7390–7407. https://doi.org/10.1002/2015JC011594

Rignot, E., Jacobs, S., Mouginot, J., & Scheuchl, B. (2013). Ice-shelf melting around Antarctica. *Science*, *341*(6143), 266–270. https://doi.org/10.1126/science.1235798

Rintoul, S. R., Silvano, A., Peña-Molino, B., van Wijk, E., Rosenberg, M., Greenbaum, J. S., & Blankenship, D. D. (2016). Ocean heat drives rapid basal melt of the Totten Ice Shelf. *Science Advances*, *2*(12), e1601610–e1601610. https://doi.org/10.1126/sciadv.1601610

Rodriguez, A. R., Mazloff, M. R., & Gille, S. T. (2016). An oceanic heat transport pathway to the Amundsen Sea Embayment. *Journal of Geophysical Research: Oceans*, *121*, 3337–3349. https://doi.org/10.1002/2015JC011402

Roquet, F., Charrassin, J.-B., Marchand, S., Boehme, L., Fedak, M., Reverdin, G., & Guinet, C. (2011). Delayed-mode calibration of hydrographic data obtained from animal-borne satellite relay data loggers. *Journal of Atmospheric and Oceanic Technology*, *28*(6), 787–801. https://doi.org/10.1175/2010JTECHO801.1

Roquet, F., Williams, G., Hindell, M. A., Harcourt, R., McMahon, C., Guinet, C., et al. (2014). A Southern Indian Ocean database of hydrographic profiles obtained with instrumented elephant seals. *Scientific Data*, *1*(40028), 1–10. https://doi.org/10.1038/sdata.2014.28

Ruan, X., Thompson, A. F., Flexas, M. M., & Sprintall, J. (2017). Contribution of topographically generated submesoscale turbulence to Southern Ocean overturning. *Nature Geoscience*, *10*(11), 840–845. https://doi.org/10.1038/ngeo3053

Ryan, S., Hattermann, T., Darelius, E., & Schröder, M. (2017). Seasonal cycle of hydrography on the eastern shelf of the Filchner Lrough, Weddell Sea, Antarctica. *Journal of Geophysical Research: Oceans*, *122*, 6437–6453. https://doi.org/10.1002/2017JC012916

Schmidtko, S., Heywood, K. J., Thompson, A. F., & Aoki, S. (2014). Multidecadal warming of Antarctic waters. *Science*, *346*(6214), 1227–1231. https://doi.org/10.1126/science.1256117

Shepherd, A., Ivins, E., Rignot, E., Smith, B., van den Broeke, M., Velicogna, I., et al. (2018). Mass balance of the Antarctic ice sheet from 1992 to 2017. *Nature*, *558*(7709), 219–222. https://doi.org/10.1038/s41586-018-0179-y

Silvano, A., Rintoul, S. R., & Herraiz-Borreguero, L. (2016). Ocean-ice shelf interaction in east Antarctica. *Oceanography*, *29*(4), 130–143.

Silvano, A., Rintoul, S. R., Peña-Molino, B., & Williams, G. D. (2017). Distribution of water masses and meltwater on the continental shelf near the Totten and Moscow University ice shelves. *Journal of Geophysical Research: Oceans*, *122*, 2050–2068. https://doi.org/10.1002/2016JC012115

Smith, R., Jones, P., Briegleb, B., Bryan, F., Danabasoglu, G., Dennis, J., et al. (2010). The Parallel Ocean Program (POP) reference manual ocean component of the Community Climate System Model (CCSM) and Community Earth System Model (CESM). *LAUR-10-01853*, *141*, 1–140.

Snow, K., Sloyan, B. M., & Rintoul, S. R. (2016). Controls on circulation, cross-shelf exchange and dense water formation in an Antarctic polynya. *Geophysical Research Letters*, *43*, 7089–7096. https://doi.org/10.1002/2016GL069479

Spence, P., Griffies, S., England, M., Hogg, A., Saenko, O. A., & Jourdain, N. C. (2014). Rapid subsurface warming and circulation changes of Antarctic coastal waters by poleward shifting winds. *Geophysical Research Letters*, *41*, 4601–4610. https://doi.org/10.1002/2014GL060613

Spence, P., Holmes, R. M., Hogg, A. M., Griffies, S. M., Stewart, K. D., & England, M. H. (2017). Localized rapid warming of west Antarctic subsurface waters by remote winds. *Nature Climate Change*, *7*(July), 1–10. https://doi.org/10.1038/nclimate3335

St-Laurent, P., Klinck, J. M., & Dinniman, M. S. (2013). On the role of coastal troughs in the circulation of warm circumpolar deep water on Antarctic shelves. *Journal of Physical Oceanography*, *43*(1), 51–64. https://doi.org/10.1175/JPO-D-11-0237.1

Steig, E., Ding, Q., Battisti, D., & Jenkins, A. (2012). Tropical forcing of circumpolar deep water inflow and outlet glacier thinning in the Amundsen Sea Embayment, West Antarctica. *Annals of Glaciology*, *53*(60), 19–28. https://doi.org/10.3189/2012AoG60A110

Stewart, A. L., Klocker, A., & Menemenlis, D. (2018). Circum-Antarctic shoreward heat transport derived from an eddy- and tide-resolving simulation. *Geophysical Research Letters*, *45*, 834–845. https://doi.org/10.1002/2017GL075677

Stewart, A. L., & Thompson, A. F. (2013). Connecting Antarctic cross-slope exchange with Southern Ocean overturning. *Journal of Physical Oceanography*, *43*(7), 1453–1471. https://doi.org/10.1175/JPO-D-12-0205.1

Stewart, A., & Thompson, A. (2015a). The neutral density temporal residual mean overturning circulation. *Ocean Modelling*, *90*, 44–56. https://doi.org/10.1016/j.ocemod.2015.03.005

Stewart, A. L., & Thompson, A. F. (2015b). Eddy-mediated transport of warm circumpolar deep water across the Antarctic shelf break. *Geophysical Research Letters*, *42*, 432–440. https://doi.org/10.1002/2014GL062281

Stewart, A. L., & Thompson, A. F. (2016). Eddy generation and jet formation via dense water outflows across the Antarctic continental slope. *Journal of Physical Oceanography*, *46*(12), 3729–3750. https://doi.org/10.1175/JPO-D-16-0145.1

Thoma, M., Jenkins, A., Holland, D., & Jacobs, S. (2008). Modelling circumpolar deep water intrusions on the Amundsen Sea continental shelf, Antarctica. *Geophysical Research Letters*, *35*, L18602. https://doi.org/10.1029/2008GL034939

Thompson, A. F., Heywood, K. J., Schmidtko, S., & Stewart, A. L. (2014). Eddy transport as a key component of the Antarctic overturning circulation. *Nature Geoscience*, *7*(12), 879–884. https://doi.org/10.1038/ngeo2289

Wåhlin, A. K., Kalén, O., Arneborg, L., Björk, G., Carvajal, G. K., Ha, H. K., et al. (2013). Variability of warm deep water inflow in a submarine trough on the Amundsen Sea shelf. *Journal of Physical Oceanography*, *43*(10), 2054–2070. https://doi.org/10.1175/JPO-D-12-0157.1

Wåhlin, A. K., Kalén, O., Assmann, K. M., Darelius, E., Ha, H. K., Kim, T. W., & Lee, S. H. (2016). Subinertial oscillations on the Amundsen Sea shelf, Antarctica. *Journal of Physical Oceanography*, *46*(9), 2573–2582. https://doi.org/10.1175/JPO-D-14-0257.1

Wåhlin, A. K., Muench, R. D., Arneborg, L., Björk, G., Ha, H. K., Lee, S. H., & Alsén, H. (2012). Some implications of Ekman layer dynamics for cross-shelf exchange in the Amundsen Sea. *Journal of Physical Oceanography*, *42*, 1461–1474. https://doi.org/10.1175/JPO-D-11-041.1

Walker, D. P., Brandon, M. A., Jenkins, A., Allen, J. T., Dowdeswell, J. A., & Evans, J. (2007). Oceanic heat transport onto the Amundsen Sea shelf through a submarine glacial trough. *Geophysical Research Letters*, *34*, L02602. https://doi.org/10.1029/2006GL028154

Walker, D. P., Jenkins, A., Assmann, K. M., Shoosmith, D. R., & Brandon, M. A. (2013). Oceanographic observations at the shelf break of the Amundsen Sea, Antarctica. *Journal of Geophysical Research: Oceans*, *118*, 2906–2918. https://doi.org/10.1002/jgrc.20212

Zhang, X., Thompson, A. F., Flexas, M. M., Roquet, F., & Bornemann, H. (2016). Circulation and meltwater distribution in the Bellingshausen Sea: From shelf break to coast. *Geophysical Research Letters*, *43*, 6402–6409. https://doi.org/10.1002/2016GL068998